Quantifying Outer- and Inner-Coordination Sphere Effects Using Uranium Redox Chemistry in Molten Salt Solutions

Marshall-Roth, Travis; MacInnes, Molly; Jordan, Aldo Michele; Piedmonte, Ida; Pace, Kristen Amanda; Adelman, Sara Linnae; Anderson, Nickolas H.; Cooley, Jason Christopher; Kozimor, Stosh Anthony; Mullis, Monica Suzanne; Mocko, Veronika; Rocha, Francisca Rein; Stein, Benjamin

To be published in: Journal of the American Chemical Society, Article 148, Vol. 16, p. 16713-16725, 2026-04-14

DOI to publisher's version: 10.1021/jacs.5c20789

Quantifying Outer- and Inner-Coordination Sphere Effects Using Uranium Redox Chemistry in Molten Salt Solutions

Travis Marshall-Roth, Molly M. MacInnes, Aldo M. Jordan, Ida D. Piedmonte, Kristen A. Pace, Sara L. Adelman, Nickolas H. Anderson,* Jason C. Cooley, Stosh A. Kozimor,* Monica S. Mullis, Veronika Mocko, Francisca R. Rocha, Benjamin W. Stein

[1] Los Alamos National Laboratory (LANL), P.O. Box 1663, Los Alamos, New Mexico, 87545, USA

* To whom correspondence should be directed, *e-mail;* nhanderson@lanl.gov, stosh@lanl.gov

LA-UR-25-29884

TABLE OF CONTENT GRAPHIC

Outer- and inner-coordination sphere effects on uranium redox chemistry were interrogated in two series of alkali halide molten salts at 850 °C by cyclic voltammetry. These data were used to develop a model for predicting redox chemistry in molten salts based on electrostatic interactions using Coulomb's Law.

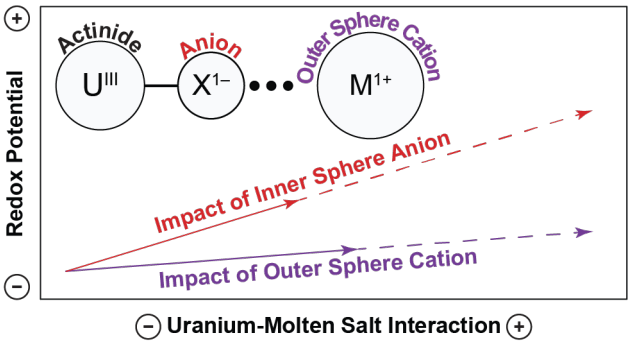

Abstract

Defining the relative influence of *intra*molecular and *inter*molecular forces is a fundamental problem in chemistry that is difficult to quantify. To address this challenge, we developed a method to evaluate the relative impact of direct chemical bonding in the inner-coordination sphere vs. effects from cations in the outer-coordination sphere by comparative analysis of uranium redox reactivity in various molten salts. We observed that outer-coordination sphere cations (M^{1+}) and inner-coordination sphere anions (X^{1-}) both affected uranium redox reactivity, with more

polarizing M^{1+} and larger X^{1-} favoring uranium in low oxidation states. Changing M^{1+} (Li, Na, K) shifted the $U^{IV} + e^{1-} \rightleftharpoons U^{III}$ ($U^{IV/III}$) and $U^{III} + 3e^{1-} \rightarrow U^{0}_{metal}$ potentials by +330 and +240 mV, respectively. Changing X^{1-} (Cl, Br, I) caused larger shifts of +440 mV for the $U^{IV/III}$ redox potential and +1060 mV for the U^{0}_{metal} deposition potential. Using Coulomb's Law, we correlated these redox potentials with electrostatic interactions between U^{III} and the molten salt. This model provided a facile way of predicting redox chemistry within molten salts.

Introduction

The chemistry community has historically struggled to characterize how *inter*molecular (e.g., hydrogen bonding, ion-dipole, ion-induced dipole, van der Waals) vs. *intra*molecular (e.g., direct chemical bonding) interactions impact the properties of an analyte. Understanding this interplay is important for accurately tuning the electronic structure, physical properties, and reactivity. Toward this end, researchers have used spectroscopic and electrochemical methods to show how direct bonding interactions influence the physics and chemistry of chemical species.[1–7] There is also literature identifying structure-to-function relationships between a compound and ions and molecules in the outer-coordination sphere. As a representative example, X-ray and neutron diffraction, optical and fluorescence spectroscopies, solution-phase NMR, and electrochemistry experiments have shown how hydrogen bonding and ionic interactions in the outer-coordination sphere impact chemical structure and in turn influence physical properties and reactivity.[8–18] Unfortunately, there are many other scenarios where outer-coordination sphere effects are hard to detect directly.[19–29] Developing approaches to observe and compare outer-coordination sphere interactions with direct chemical bonding in the inner sphere would be valuable. It would provide an opportunity to tune the structure, reactivity, and physical properties of analytes by manipulating

both the nature of direct chemical bonds as well as the molecules and ions present in the outer-coordination sphere.

In addressing this challenge, we developed a quantitative method to compare the impact of outer-coordination sphere and direct chemical bonding interactions on the electron transfer chemistry accessible to a metal ion. Our approach used molten salts to provide a chemical environment where direct chemical bonding interactions and outer coordination sphere effects could be systematically varied by changing the molten salt identity. The relative impact of the outer and inner coordination spheres on metal redox chemistry was quantified using high-temperature (850 ºC) electrochemical measurements. After surveying the literature, we identified uranium as being well-suited for study. That determination was influenced by decades of literature on uranium redox reactivity and speciation in molten salts focused on molten salt nuclear reactor development and actinide electrorefining.[30–35] Based on these data, we proposed that if the impact of the outer-coordination sphere cations (M^{1+} = alkali metal) and inner-coordination sphere anions (X^{1-} = halide) were similar in magnitude, then U^{n+} redox reactivity could be controlled by changing the identities of the two molten salt components. This hypothesis was tested by evaluating the influence of the inner- (U^{n+}–X^{1-}) and outer- ($U^{n+}\cdots M^{1+}$) coordination spheres on the potentials associated with the $U^{IV} + e^{1-} \rightleftharpoons U^{III}$ ($U^{IV/III}$) and $U^{III} + 3e^{1-} \rightarrow U^{0}_{metal}$ (U^{0}_{metal} deposition) electron transfer reactions.

The approach outlined herein offers a novel and methodical way to investigate inner- (U^{n+}–X^{1-}) vs. outer- ($U^{n+}\cdots M^{1+}$) coordination sphere interactions. Note that the U^{n+}–X^{1-} and $U^{n+}\cdots M^{1+}$ notation provides effective descriptors for interactions present in molten salts do not covey detailed information regarding speciation. For example, when U^{IV} is dissolved in molten NaCl, the inner U^{IV} coordination sphere is comprised of Cl^{1-} anions and the outer-coordination sphere is largely

dominated by Na^{1+} interactions, provided the uranium concentration is low (Scheme 1).[36] Changing the molten salt from NaCl to KCl allows the relative impact of M^{1+} in the outer-coordination sphere to be evaluated in terms of the differences between U^{IV}–Cl^{1-}···Na^{1+} and U^{IV}–Cl^{1-}···K^{1+}, while maintaining the inner-coordination sphere anion constant at Cl^{1-}. Similarly, changing the molten salt from KCl to KBr allows the relative impact of X^{1-} in the inner-coordination sphere to be evaluated as a function of U^{IV}–Cl^{1-}···K^{1+} and U^{IV}–Br^{1-}···K^{1+}, while keeping the outer-coordination sphere cation constant at K^{1+}. Obtaining similar control over U^{n+}–X^{1-} vs. U^{n+}···M^{1+} interactions would be difficult to achieve in conventional room temperature organic and aqueous solutions. An equivalent study in aqueous media would require replacing the oxygen atom in H_2O molecules with sulfur or selenium, which is impractical because of the toxicity and volatility of H_2S and H_2Se. Hence, the advantage of the molten salt matrix.

Herein, we used high-temperature cyclic voltammetry to characterize how the $U^{IV} + e^{1-} \rightleftharpoons U^{III}$ ($U^{IV/III}$) and $U^{III} + 3e^{1-} \longrightarrow U^0_{metal}$ (U^0_{metal} deposition) redox processes varied as a function of either the outer-coordination sphere alkali metal cation (M^{1+} = Li, Na, and K) or the inner-coordination sphere halide anion (X^{1-} = Cl, Br, and I). The outer-coordination sphere effect was evaluated by holding X^{1-} constant at Cl^{1-} and changing the molten salt from LiCl to NaCl to KCl. In the same vein, the inner-coordination sphere anion effect was examined by maintaining M^{1+} as K^{1+} and changing the molten salt from KCl to KBr to KI. Critical to our approach was a referencing method we developed for comparing redox potentials in different molten salt solvents (e.g. NaCl vs. KCl).

We discovered that the $U^{IV/III}$ and U^0_{metal} deposition redox reactions were sensitive to both X^{1-} and M^{1+} within the U^{n+}–X^{1-}···M^{1+} framework. Moving down the halide series by one row (changing X^{1-} from Cl^{1-} to Br^{1-} to I^{1-}) shifted the $U^{IV/III}$ half-wave potential ($E_{½}$) and the U^0_{metal}

deposition to a larger extent than descending the alkali metal series (Li^{1+} to Na^{1+} to K^{1+}). We also observed that the U^0_{metal} deposition process was more sensitive to X^{1-} than the $U^{IV/III}$ redox reaction. These findings suggested that polarizing M^{1+} cations (Li^{1+} vs. K^{1+}) stabilized uranium in low-oxidation states and small X^{1-} anions (Cl^{1-} vs. I^{1-}) stabilized uranium in high-oxidation states. Based on these observations, we developed a method for predicting redox potentials in molten salts. This model correlated the $U^{IV/III}$ half-wave potential ($E_{½}$) and U^0_{metal} deposition potentials with the Coulombic electrostatic interaction between U^{III} and the molten salt components (defined herein as the U^{III}–molten salt interaction parameters). Although more data are needed to validate this model and demonstrate its applicability beyond uranium, our approach succeeded in capturing the relative influence of the inner-coordination sphere anions (X^{1-}) and outer-coordination sphere cations (M^{1+}) on two uranium redox events. It also provided a straightforward way to predict how redox potentials varied as a function of molten salt identity and could aid technologies that rely on molten salt solutions, such as next-generation molten salt nuclear reactors and actinide electrorefining methodologies.

Results and Discussion

Preparation of U^{III}-Containing Molten Salt Solutions. Molten salt solutions were generated by heating an anhydrous alkali halide salt (LiCl, NaCl, KCl, KBr, or KI) in a quartz tube to 850 °C using a custom cylindrical furnace housed within an argon-filled glovebox.[37] All molten salt studies described herein were conducted at 850 ºC because at this temperature all five salts were liquid, which facilitated direct comparisons. The electrochemical experiments employed a Ni/NiX_2 (X = Cl, Br, or I) reference electrode alongside glassy carbon rod working and counter electrodes. After reaching 850 °C, the cell was allowed to equilibrate until the open circuit potential of the cell stabilized (~2 h). Subsequently, cyclic voltammograms were recorded to ensure the cell was

operating at low resistance values (1–2 Ω). These measurements also characterized the electrochemical solvent window and confirmed that no extraneous redox-active species were present before uranium was introduced.

Our approach for generating U^{III} molten salt solutions was inspired by a few examples already in the literature.[32–34] In our procedure, the two glassy carbon rods used to characterize electrochemical responses from pristine molten salts were replaced with two metallic uranium (U^0_{metal}) electrodes (Scheme 2). The U^{III} analyte was then stripped from the U^0_{metal} rods into the molten salt solution by applying an oxidizing potential at a constant current of −100 mA (Scheme 2, left; see Supporting Information). Sufficient charge, monitored using chronopotentiometry, was passed to generate U^{III}-containing solutions. Independent analysis using inductively coupled plasma atomic emission spectroscopy (ICP-AES) showed these salts contained 0.04–0.76 wt.% (*vide infra*), which was less than predicted based on the chronopotentiometry measurements. Finally, the U^0_{metal} rods were exchanged for glassy carbon electrodes and electrochemical experiments on U^{III} were conducted. This method was quite different from most of the studies in the field, where U^{III} is introduced by adding independently synthesized uranium halides or oxidizing uranium metal by adding metal chlorides.[35,38–40]

Characterizing the U^{III} stripping procedure indicated that the chronopotentiometry measurements overestimated the quantities of U^{III} introduced into each salt. For example, the amount of uranium present in the molten salt was quantified by cooling the U^{III}-containing salts to room temperature, dissolving the sample in aqueous media, and quantifying uranium content using ICP-AES. These results indicated that the stripping procedure generated molten salt solutions whose U^{III} content ranged from 0.04 to 0.76 wt.%, depending on salt identity, which corresponded to Faradaic efficiencies of 4–76% for U^{III} stripping (see Table 1). A potential reason for the large

variation of U^{III} stripping efficiencies was associated with potential side reactions that likely occur at the working and counter electrodes. Side reactions would also account for the disconnect between the charged passed and the amount of U^{III} introduced into the molten salt. Efforts are underway to understand the variation in U^{III} stripping efficiency as a function of salt identity and optimize the experimental conditions and electrochemical setup (i.e., divided cells) to maximize the efficiency of U^{III} stripping.

We concluded that our procedure for generating uranium molten salts primarily introduced U^{III} into the molten salt matrix, rather than U^{IV} or a mixture of U^{III} and U^{IV}. Consistent with that notion were reports in the literature that also found U^{III} to be the primary product from U^0_{metal} stripping processes.[32–34] Generating U^{III} under our experimental conditions makes intuitive sense because the negative potential applied during the stripping process was bracketed by the $U^{III} + 3e^{1-} \rightarrow U^0_{metal}$ reduction and $U^{III} \rightarrow U^{IV} + e^{1-}$ oxidation potentials. Ensuing electrochemical measurements were also consistent with this assignment. First, resting potentials for uranium-containing salts were between the $U^{III} + 3e^{1-} \rightarrow U^0_{metal}$ reduction and $U^{III} \rightarrow U^{IV} + e^{1-}$ oxidation potentials, consistent with U^{III} formation. Second, cyclic voltammograms that started at the resting potential of the cell and scanned positive produced an oxidation wave (U^{IV} generation) whose peak amplitude and area were similar to the reduction wave obtained on the return scan. In general, if U^{IV} was present at the resting potential of the cell, then that oxidation peak would not be observed. In addition, if the molten salt contained a substantial mixture of U^{III} and U^{IV}, then the peak amplitude and area for the oxidation and reduction waves would not be equivalent. Taken as a whole, these data are all consistent with U^{III} being the primary uranium product from our uranium metal stripping procedure.

The electrochemical oxidation of metallic uranium deployed herein conferred several advantages over those that relied on adding independently synthesized uranium halides. For instance, oxidative dissolution allowed uranium-containing solutions to be generated in several minutes and the U^0_{metal} rods could be used multiple times. In contrast, the synthetic procedures for unsolvated trivalent and tetravalent uranium halide salts can be time consuming[41] and – at times – introduce uranium oxide, uranium oxyhalide, and organic impurities that convolute electrochemical results.[42]

Uranium Stripping Method Validation. Our electrochemical method for preparing U^{III} molten salt solutions was validated by reproducing some published electrochemical data collected in eutectic molten salts that contained independently synthesized UCl_3.[35,43] To achieve this goal, we stripped U^{III} from U^0_{metal} rods into a LiCl and KCl (46 wt.% LiCl to 54 wt.% KCl) eutectic at 500 ºC. Cyclic voltammetry data collected using U^{III} solutions prepared by electrochemical oxidation of U^0_{metal} were in excellent agreement with published measurements made on a uranium molten salt solution comprised of independently synthesized UCl_3, LiCl, and KCl (Figure 1, *bottom trace*).[35,43] We observed the expected $U^{IV/III}$ redox wave ($U^{IV} + e^{1-} \rightleftharpoons U^{III}$, orange) as well as characteristic features previously attributed to U^0_{metal} deposition ($U^{III} + 3e^{1-} \rightarrow U^0_{metal}$, $I_{cathode}$ and $II_{cathode}$, blue) and U^{III} stripping ($U^0_{metal} \rightarrow U^{III} + 3e^{1-}$, I_{anode} and II_{anode}, green). The deposition $I_{cathode}$ and stripping I_{anode} waves were consistent with underpotential deposition and stripping of monolayer quantities of uranium metal from the working electrode.[43,44]

Temperature-Dependent Uranium Redox Features in a LiCl–KCl Eutectic. Cyclic voltammograms recorded between 600 and 800 °C using the same eutectic enabled us to

characterize how temperature influenced the $U^{IV/III}$, U^{0}_{metal} deposition, and U^{III} stripping processes. Results from the measurements made in eutectic solutions provided a framework for interpreting data subsequently obtained in pure alkali halide salt solutions. While the voltammograms collected at 600, 700, and 800 °C showed similar redox events to those observed at 500 °C, we observed several notable differences (Figure 1). For example, the potentials associated with the uranium electron transfer events changed substantially with temperature. The temperature-induced potential shifts were distinct for the three uranium redox events: 140 mV (0.5 mV/°C) for $U^{IV/III}$, 170 mV (0.7 mV/°C) for U^{0}_{metal} deposition ($I_{cathode}$), and 20 mV (0.2 mV/°C) for U^{0}_{metal} deposition ($II_{cathode}$). Increasing the temperature from 500 to 800 °C also shifted the alkali reduction process positive by 200 mV and obscured the $II_{cathode}$ U^{0}_{metal} deposition event.

Multiple factors were likely responsible for these changes. Increased temperatures could lead to larger diffusion coefficients, lower solution viscosity and dielectric constants,[45,46] and higher electron transfer rates. We also suspected that the temperature dependence of the uranium electron transfer reactions contributed as well as the temperature dependence of the electron transfer reaction associated with the $Ni^{II/0}$ reference potential. To characterize the relative magnitudes of the temperature dependence of the uranium and $Ni^{II/0}$ redox reactions, the stability of the $Ni^{II/0}$ reference electrode was analyzed over time (2 h) as the temperature changed from 800 to 500 ºC. This time interval was substantially longer than that required to acquire cyclic voltammograms. We observed a maximum shift of 39 mV for the reference electrode (see the Supporting Information). This shift was slightly larger than the +20 mV shift predicted by the Nernst equation for a 300 ºC temperature change.[47] Hence, the 39 mV shift likely also reflected that increasing temperature changed Ni^{II} activity, speciation, and concentration in the reference electrode. The drift in the $Ni^{II/0}$ reference potential was also substantially smaller than the shifts observed for the

$U^{IV/III}$ (140 mV) and U^0_{metal} (170 mV; $I_{cathode}$) deposition events, indicating that those two uranium reactions were impacted by temperature to a larger extent than the $Ni^{II/0}$ reference process.

The electrochemical measurements also revealed substantial changes in the U^{III} stripping events (I_{anode} and II_{anode}). The potentials for these electron transfer processes shifted negative by 140 mV (−0.5 mV/°C over 500–800 °C) and 80 mV (−0.4 mV/°C over 500–700 °C). At 700 and 800 °C, I_{anode} also broadened and split into three separate peaks (I_{a1}, I_{a2}, and I_{a3}). Current efforts are focused on better characterizing the origin of the multiple peaks. Likely candidates could be oxidation of distinct uranium facets or oxidation of surface-adsorbed low-oxidation state uranium species.[44,48,49] Differential pulse voltammetry experiments suggested that I_{a1}, I_{a2}, and I_{a3} involved one-electron transfer steps, consistent with multiple oxidation steps of surface-bound uranium species leading to dissolution of U^{III} from the electrode surface (see the Supporting Information). Given that the U^{III} stripping behavior in a LiCl and KCl eutectic was more complex at 800 ºC than at the lower temperatures, it was not surprising to observe similarly complicated U^{III} stripping in the pure alkali halide melts (*vide infra*). As such, we have focused this study exclusively on the $U^{IV/III}$ redox reaction and U^0_{metal} deposition process in pure alkali halide salts. A follow-on publication will center on characterizing the high-temperature U^{III} stripping processes in more detail.

Referencing Electrode Potentials in Pure Molten Salt Solutions. A referencing system was developed to compare the potentials for the $U^{IV/III}$ and U^0_{metal} deposition redox processes in KCl, NaCl, LiCl, KBr, and KI salt solutions and at a common temperature where all five salts were liquid (850 ºC). We employed a $Ni^{II/0}$ reference electrode composed of a Ni^0 wire encased in a mullite tube. The tube also contained a mixture of NiX_2 (1 wt.%) in an alkali metal salt (MX) that

had been ground with a mortar and pestle prior to use. Although other reference systems have been reported in molten salts,[50–56] the $Ni^{II/0}$ referencing system displayed rapid kinetics, Nernstian scaling behavior, and stability toward reference potential drift in molten chloride or fluoride salts on the order of 5 mV/day.[53,57,58]

To compare uranium redox potentials obtained in the five different NaCl, KCl, LiCl, KBr, and KI salt solutions it was necessary to develop potential correction factors for the $Ni^{II/0}$ reference redox couple. A high-level description is included herein and more detailed information about the referencing approach and associated analysis of the $Ni^{II/0}$ redox process can be found in the Supporting Information. These potential correction factors were determined in three steps. In step 1, the $Ni^{II/0}$ redox couple was recorded using a glassy carbon (GC) working electrode (*working*) and a $Ni^{II/0}$ reference electrode (*reference*). In these experiments, the working and reference compartments were filled with $NiCl_2$ and KCl: GC-$Ni^0_{(s),working}|NiCl_{2(KCl),working}||NiCl_{2(KCl),reference}|Ni^0_{(s),reference}$. In step 2, the $Ni^{II/0}$ redox couple was characterized in every other MX salt (e.g. LiCl, NaCl, KBr, or KI). In these experiments the $Ni^{II/0}$ redox potential was measured using a glassy carbon (GC) working electrode and a $Ni^{II/0}$ reference electrode, similar to step 1. Another similarity between step 1 and step 2 was that the NiX_2 and MX salts in the working and reference compartments were the same: GC-$Ni^0_{(s),working}|NiX_{2(MX),working}||NiX_{2(MX),reference}|Ni^0_{(s),reference}$. For example, for the KBr experiments, the working and reference compartment contained $NiBr_2$ and KBr. In step 3, the $Ni^{II/0}$ redox reaction was characterized again across the NiX_2 and MX series, as in step 2; however, the salts in the referencing compartment were not the same as those in the working compartment. Instead, in step 3 the reference compartment always contained $NiCl_2$ and KCl: GC-$Ni^0_{(s),working}|NiX_{2(MX)}||NiCl_{2(KCl),reference}|Ni^0_{(s),reference}$. For example, for KBr, the working

compartment was filled with $NiBr_2$ and KBr and the reference compartment was filled with $NiCl_2$ and KCl. These three series of experiments provided the necessary data for (*1*) establishing potential corrections for membrane potentials across the mullite membrane of the reference electrode, (*2*) nonidealities in the interactions of the Ni^{II} and M^{1+} cations with the ion-conducting sites in the mullite ceramic, and (*3*) the thermochemical differences in salt potentials at 850 °C were derived (see the Supporting Information).[59–64] The analyses provided potential correction factors that enabled measurements made in NaCl, LiCl, KBr, and KI solutions to be plotted on the same potential scale used for KCl solutions: +0.00 V in KCl, +0.18 ± 0.03 V in NaCl, +0.20 ± 0.05 V in LiCl, +0.28 ± 0.01 V in KBr, and +0.77 ± 0.04 V in KI.

Dependence of $U^{IV/III}$ Redox Potentials on Molten Salt Identity. The $U^{IV/III}$ redox couple varied as a function of the outer-coordination sphere alkali metal cation as well as the inner-coordination sphere halide anion. Cyclic voltammograms from KCl solutions containing U^{III} displayed an electron transfer event whose half-wave potential ($E_{½}$) was −0.12 V vs. $Ni^{II/0}$. This redox event was reasonably assigned to the $U^{IV/III}$ redox couple based on its position, shape, and diffusion-dependence (see the Supporting Information).[35,43] Changing M^{1+} from K^{1+} to Na^{1+} to Li^{1+} while maintaining X^{1-} as Cl^{1-} moved the $U^{IV/III}$ $E_{½}$ redox potentials positive by up to 0.33 ± 0.11 V: −0.12 ± 0.02 V in KCl, 0.13 ± 0.05 V in NaCl, and 0.21 ± 0.09 V in LiCl (Figure 2, top). Changing X^{1-} from Cl^{1-} to Br^{1-} to I^{1-} and holding M^{1+} constant as K^{1+} shifted the $U^{IV/III}$ redox potentials positive as well. Moving from Cl^{1-} to Br^{1-} shifted $E_{½}$ by 0.44 ± 0.06 V: −0.12 ± 0.02 V in KCl and 0.32 ± 0.04 V in KBr (Figure 2, bottom). In KI the $U^{IV/III}$ redox event was even more positive and was obscured behind the iodide oxidation process, suggesting that $E_{½}$ was greater than 0.32 V. This indicated that U^{IV} (presumably as UI_n^{4-n}) was a stronger oxidant than I_2 in the KI

solvent. As expected, changing the halide identity had a more pronounced effect than changing the alkali metal identity, with the $U^{IV/III}$ $E_{½}$ potential shifting across the Cl^{1-}, Br^{1-}, and I^{1-} series by more than was observed across the Li^{1+}, Na^{1+}, and K^{1+} series.

Dependence of U^{III} Diffusion Coefficients on Molten Salt Identity. The molten salt identity also impacted uranium diffusion through the salt solution. For instance, diffusion coefficients for the U^{III} species were calculated from the cathodic peak current of the $U^{IV/III}$ redox wave at a macroscopic cylindrical electrode using the Randles-Ševčík equation with a scan rate of 100 mV s^{-1} and an electron transfer number of one (z = 1). An effective electrode radius was calculated and used to modify the electrode area employed in the Randles-Ševčík relationship to account for minor contributions from radial diffusion at a macroscopic cylindrical electrode.[65–67] The surface area of the working electrode in each salt was estimated from the salt mass and density at the experimental temperature for the cell geometry and dimensions (see Supporting Information for calculation details).[45,68] The diffusion coefficients for U^{III} ranged from 0.20 to 1.45 × 10^{-5} cm^2 s^{-1}, and varied based on the molten salt identity: LiCl = (0.83 ± 0.29) × 10^{-5}, NaCl = (1.28 ± 0.76) × 10^{-5}, KCl = (1.45 ± 0.37) × 10^{-5}, and KBr = (0.20 ± 0.10) × 10^{-5} in agreement with published values determined using the $U^{IV/III}$ couple.[43,49,69–72] The relationship between the diffusion coefficients and the ionic radii from molten salt cations and anions were best described as linear (see the Supporting Information). The slopes for the fitted lines were (0.96 ± 0.15) × 10^{-5} cm^2 s^{-1} $Å^{-1}$ for the molten salt cation series and (−8.32) × 10^{-5} cm^2 s^{-1} $Å^{-1}$ for the molten salt anion series. These analyses demonstrated that U^{III} diffusion through molten salts was impacted to a larger extent by the X^{1-} anions than by the M^{1+} cations.

It was difficult to rationalize the diffusion coefficient results by only considering the viscosity of the molten salt solution. Hence, we speculated that uranium speciation and uranium-solvent interactions also contributed. For example, within the alkali chloride series, the U^{III} diffusion coefficient was smallest in LiCl, intermediate in NaCl, and largest in KCl. Solvent viscosity at 850 °C decreased in the order of NaCl>KCl>LiCl,[73] and thus does not explain the observed trend in diffusion coefficients. Interactions between UCl_n^{3-n} species and more polarizing M^{1+} cations, like Li^{1+}, likely slowed U^{III} diffusion compared to interactions with less polarizing cations, like K^{1+}. Similar observations have been reported in aqueous media, such that larger solvation shells around more polarizing ions in aqueous solutions lead to slower diffusion rates.[74] Differences in the molten salt viscosity also did not account for the U^{III} diffusion coefficients measured in KBr and KCl. Substantially smaller diffusion coefficients were observed for U^{III} in KBr than in KCl, but KBr is only slightly more viscous than KCl at 850 °C. [73] It seems possible that movement of the larger UBr_n^{3-n} ions were impacted by the molten solvent identity to a different extent than the smaller UCl_n^{3-n} analogues. Experimental and computational efforts are currently underway to interrogate the impact of cations and anions on U^{III} diffusion rates.

Dependence of U^0_{metal} Deposition Potentials on Molten Salt Identity. As with the $U^{IV/III}$ redox couples, the peak potentials observed for the U^0_{metal} deposition processes also varied as a function of the molten salt cation and anion identities. Voltammetry traces collected over a wide potential range at 850 °C in each alkali halide molten salt displayed U^0_{metal} deposition peaks denoted as $I_{cathode}$ (Figure 3). There were also U^{III} stripping features (I_{a1}, I_{a2}, and I_{a3}), that were reminiscent of those observed in the LiCl–KCl eutectic (Figure 1). Electrochemical analyses suggested that $I_{cathode}$ was a three-electron transfer process (see the Supporting Information), which

would be consistent with the three electron $U^{III} + 3e^{1-} \rightarrow U^0_{metal}$ deposition reaction. A more detailed analysis of these U^{III} stripping features will be the focus of a subsequent report. The U^0_{metal} deposition peak potential (E_p) in the alkali chloride melts varied by 0.24 ± 0.10 V: −1.24 ± 0.02 V in KCl, −1.03 ± 0.05 V in NaCl, and −1.00 ± 0.08 V in LiCl. More substantial changes in U^0_{metal} deposition potentials were observed when the molten salt halide was changed. For example, Figure 3 showcased how the U^0_{metal} deposition potentials varied by 1.06 ± 0.13 V as X^{1-} changed from Cl^{1-} (−1.24 ± 0.02 V in KCl), to Br^{1-} (−0.84 ± 0.03 V in KBr), to I^{1-} (−0.18 ± 0.11 V in KI).

Changing the molten salt cations and anions shifted U^0_{metal} deposition potentials in the same manner as the $U^{IV/III}$ $E_{½}$ potentials, however the magnitude of these changes varied. As was true for $U^{IV/III}$ $E_{½}$ potentials, changing the molten salt cations moved the U^0_{metal} deposition potential positive (by 240 mV) as the M^{1+} polarization power increased. A similarly positive shift of 330 mV was observed for the $U^{IV/III}$ $E_{½}$ potential across the Li^{1+} to Na^{1+} to K^{1+} series. In contrast, changing the molten salt anion from Cl^{1-} to Br^{1-} to I^{1-} shifted the U^0_{metal} deposition potential far more than the $U^{IV/III}$ redox reactions (1060 vs. 440 mV). We rationalized this observation as a reflection of the chemical processes associated with these very different electron transfer events. The one electron $U^{IV/III}$ redox event likely involved some reorganizing of the inner-coordination sphere anions and outer-coordination sphere cations and possible changes in X^{1-} coordination number. In contrast, reducing UX_n^{3-n} to U^0_{metal} involved breaking all the U–X bonds, transferring three electrons to the U^{III} trication, and deposition of U^0_{metal} on the electrode surface. Within this context, it seemed reasonable that the nature of the X^{1-} anions and U–X bonds would impact the U^0_{metal} deposition process to a larger extent than the $U^{IV/III}$ redox reaction.

Predicting Uranium Redox Potentials with an Electrostatic Model. To generate a method for predicting how $U^{IV/III}$ $E_{½}$ and U^{0}_{metal} deposition peak potentials varied as a function of molten salt identity, we developed a model that correlated the potentials in each salt with a U^{III}–molten salt "interaction parameter." The value of the interaction parameter was the sum of the electrostatic interactions between U^{III}, the inner-coordination sphere X^{1-} anion, and the outer-coordination sphere M^{1+} cation. Coulomb's Law was used to approximate each interaction and an interaction parameter was calculated by summing the attractive and repulsive component interactions experienced by U^{III} in the primary U^{III}–X^{1-} and secondary U^{III}–X^{1-}···M^{1+} solvation shells (Scheme 3). The attractive component was dominated by the inner-coordination sphere U^{III}–X^{1-} interaction, while the repulsive component was dominated by the outer-coordination sphere U^{III}···M^{1+} interaction. The model also included attenuation of the U^{III}–X^{1-} attractive component by the outer-coordination sphere M^{1+} cation via X^{1-}···M^{1+} interactions (Scheme 3, left) and lowering of the U^{III}···M^{1+} repulsive interaction from charge shielding by X^{1-} (Scheme 3, right). In all cases, the effective ionic radii for six-coordinate ions[75] were used to define the distances between the point charges involved and the exact solvation structure and uranium coordination numbers were explicitly ignored. Hence, U^{III}–X^{1-} and U^{III}···M^{1+} provided convenient descriptors for the fundamental electrostatic interactions between uranium, the halide, and the alkali metal cation. They did not imply specific uranium speciation or reflect aspects of the complicated and dynamic coordination chemistry accessible to U^{III}, X^{1-}, and M^{1+} within a molten salt. Within this framework, large and negative interaction parameters indicated that the U^{III}–X^{1-} attractive interaction was larger than the U^{III}···M^{1+} repulsive interaction. Conversely, large positive interaction parameters indicated that the U^{III}···M^{1+} repulsive interaction was larger than the U^{III}–X^{1-} attractive interaction. Finally, an interaction parameter that approached zero indicated that the

U^{III}–X^{1-} attractive interaction was similar in magnitude to the repulsive $U^{III}\cdots M^{1+}$ interaction. Hence, this interaction parameter can be used to predict if the inner sphere X^{1-} anion or outer sphere M^{1+} cation will be the primary director of uranium redox chemistry in a given molten salt solution. More details about the model can be found in the Supporting Information.

Figures 4 and 5 demonstrated that changing the molten salt cation impacted the uranium redox processes in a manner that could be predicted using our interaction parameter model. Linear relationships between the U^{III}–molten salt interaction parameters for each salt and the measured $U^{IV/III}$ $E_{½}$ and U^0_{metal} deposition potentials were observed as the outer-coordination sphere cation changed from Li^{1+} to Na^{1+} to K^{1+}. The positive correlation slopes of 5.00 ± 0.06 ($U^{IV/III}$ $E_{½}$) and 3.70 ± 0.07 (U^0_{metal} deposition potential) suggested that more polarizing cations in the secondary uranium coordination sphere favored formation of lower uranium oxidation states. Here, polarizing power is defined as the oxidation state of the cation divided by the square of its ionic radius.[76–78] We rationalized these results in the following way. Increasing the polarization power of the outer-coordination sphere molten salt cation from K^{1+} to Na^{1+} to Li^{1+} withdrew electron density from uranium across the $U–X^{1-}\cdots M^{1+}$ linkage and shifted the $U^{IV/III}$ $E_{½}$ redox and U^0_{metal} deposition potentials positive. Hence, moving from KCl to NaCl to LiCl solvents stabilized formation of U^{III} (more electron rich) over U^{IV} (more electron deficient) and made conversion of U^{III} to U^0_{metal} more favorable. A similar rationale was previously invoked to explain how $Eu^{III/II}$, $Yb^{III/II}$, and $Sm^{III/II}$ $E_{½}$ potentials depended on molten salt identity and was consistent with the "optical basicity scale" concept introduced to explain ionic interactions in glass and molten salt matrices.[37,79,80]

Analogous linear relationships were also observed between the U^{III}–molten salt interaction parameters and the measured $U^{IV/III}$ $E_{½}$ and U^0_{metal} deposition potentials as the inner-coordination sphere anion changed from Cl^{1-} to Br^{1-} to I^{1-} (Figures 4 and 5). The correlation slopes were

determined to be 19.18 ($U^{IV/III}$ $E_{½}$) and 20.29 ± 0.05 (U^{0}_{metal} deposition potential). For the $U^{IV/III}$ redox reactions, the linear correlation was extrapolated beyond KBr to predict an estimated $E_{½}$ value in molten KI, even though that redox potential could not be determined experimentally (Figure 2). The calculated $U^{IV/III}$ $E_{½}$ potential in KI was 0.89 V, which was plausible and would be obscured behind the I^{1-} oxidation process. Given that the U–X^{1-} and U···M^{1+} interactions are fundamentally different, it did not make sense to use the concept of polarization power to rationalize the impact of X^{1-} on the $U^{IV/III}$ $E_{½}$ and U^{0}_{metal} deposition potentials. Instead, the potential seemed to correlate with the principal quantum number associated with the X^{1-} anion valence orbitals. Moving from 2*p* to 3*p* to 4*p* (Cl^{1-} to Br^{1-} to I^{1-}) favored formation of U^{III} over U^{IV} and made the U^{0}_{metal} deposition process more accessible. It is tempting to rationalize these findings by invoking that orbital mixing interactions between the U^{n+} cation and the X^{1-} withdrew electron density from the U^{n+} cation to support low oxidation state U^{III} species. However, we have refrained from doing so at this time and are conducting calculations to substantiate or refute the existence of electronic structure-to function-relationships for the observed redox reactivity.

Despite the apparent utility of the electrostatic interaction model for predicting $U^{IV/III}$ $E_{½}$ and U^{0}_{metal} deposition potentials, there are notable caveats that must be mentioned. The model ignores key factors that can influence electron transfer reactivity. It does not consider covalent U^{n+}–X^{1-} or X^{1-}–M^{1+} bonding interactions and only reflects the ionic character of the solvation interactions of U^{III} in different molten salts. It also ignores uranium solvation environments,[81,82] coordination numbers,[83,84] and speciation details. Despite these omissions, the model was useful because it accurately described variations in $U^{IV/III}$ $E_{½}$ and U^{0}_{metal} deposition potentials as a function of molten salt identity in five different molten salt solutions without the need for sophisticated calculations. The uranium-molten salt interaction parameters also scaled with the U^{III}-diffusion coefficients

where more destabilizing $U^{III}\cdots M^{1+}$ interactions (i.e. $U^{III}\cdots Li^{1+}$) and weaker $U^{III}–X^{1-}$ interactions (i.e. $U^{III}–Br^{1-}$) both limited U^{III} diffusion, likely from increased solution ordering or weak U^{III}-halide attraction. The general applicability of the model is being expanded to include other actinides and a wider variety of molten salts, including molten salts containing +2 and +3 cations. At the same time, more advanced models are being developed that will allow actinide molten salt redox reactivity to be better explained and predicted by incorporating electronic structure and bonding, coordination chemistry, and molecular dynamics. Essential for this computational effort is our experimental validation campaign focused on better characterizing actinide speciation in molten salts.

Outlook

In this study, molten salts and high temperature electrochemical techniques were used to evaluate the dependence of $U^{IV/III}$ $E_{½}$ and U^0_{metal} deposition potentials on M^{1+} cations in the uranium outer-coordination sphere vs. X^{1-} anions directly bound to uranium in the inner-coordination sphere. In raw potential terms, the impacts of both M^{1+} and X^{1-} on the uranium potentials were substantial, the potentials for both electron transfer reactions were shifted positive by hundreds of millivolts. In alkali chlorides, changing the M^{1+} cation identity from K^{1+} to Na^{1+} to Li^{1+} shifted the $U^{IV/III}$ redox potentials positive by 330 mV and the U^0_{metal} deposition potential by 240 mV. We rationalized this observation by considering the polarizing power of M^{1+}, such that more polarizing cations (e.g. Li^{1+}) removed electron density from U^{n+} across the $U^{n+}–X^{1-}\cdots M^{1+}$ linkage and stabilized electron-rich low oxidation state species. These data suggested that U^{III} would be a stronger reducing agent when the outer-coordination sphere M^{1+} cations were weakly polarizing and that electrochemically generating U^0_{metal} would be easier in molten salts that contained strongly polarizing outer-coordination sphere M^{1+} cations.

Changing the X^{1-} ligand directly bound to the U^{n+} cation from Cl^{1-} to Br^{1-} to I^{1-} had a more substantial impact on the uranium redox processes than changing M^{1+} from Li^{1+} to Na^{1+} to K^{1+}. For instance, in KX salts, descending the halide series shifted the $U^{IV/III}$ redox potential by 440 mV and the U^0_{metal} deposition potential by 1060 mV. These data highlighted that the X^{1-} identity had more influence over the U^0_{metal} deposition process than the $U^{IV/III}$ redox reaction, consistent with more extensive bond breakage and solvent reorganization during U^0_{metal} deposition. This observation agreed with synthetic observations that $U^{IV}Cl_4$ is more stable than $U^{III}Cl_3$ and $U^{IV}I_4$ is less stable than $U^{IV}I_3$.[85] We correlated this X^{1-} anion induced potential shift with the principal quantum number associated with halide valence orbitals, such that Cl^{1-} (2*p*-valence orbitals) favored formation of U^{IV} and I^{1-} (5*p*-valence orbitals) favored formation of U^{III}. It seemed possible that the nature of the X^{1-} valence orbitals impacted U^{n+}–X^{1-} orbital mixing and that these electronic structure changes were responsible for the observed stability of U^{IV} vs. U^{III}. Hence, a theoretical investigation on this topic is underway. Within this context, we concluded that U^{III} should be a stronger reducing agent when the inner-coordination sphere X^{1-} anion was Cl^{1-} vs. I^{1-} and that U^0_{metal} would be more easily prepared in molten salts that have heavier halogens.

Critical to this study was a reliable method for referencing electrochemical measurements made in different molten salts. We acknowledge both the strengths and weaknesses of this approach. On the positive side, the convenient and straightforward nature of the method allowed for comparative analysis of redox potentials that were measured as a function of molten salt identity. On the other hand, the method required additional experimental validation to refine the potential corrections and introduced uncertainty for measured redox potentials associated with the referencing system. Despite these limitations, we envision that this approach will aid others in

comparing electrochemical measurements in a wider range of molten salt solutions and inspire improvements to the method.

To rationalize and predict how U^{III} redox potentials varied as a function of molten salt identity, we developed an electrostatic interaction model based on Coulomb's Law. Hence, we calculated a series of U^{III}–molten salt interaction parameters by summing the electrostatic attractive $U–X^{1–}$ and repulsive $U\cdots M^{1+}$ interactions in each salt. The $U^{IV/III}$ $E_{½}$ and U^{0}_{metal} deposition potentials both correlated linearly with the U^{III}-molten salt interaction parameters, allowing uranium redox potentials to be predicted in various molten salts. Current experimental efforts are focused on improving the robustness and generality of our model for other actinides in a wider array of molten salts. We are also developing more sophisticated computational methods for predicting and understanding actinide speciation, electronic structure, and redox chemistry within molten salt solutions.

Summary

As a whole, this molten salt study advanced understanding of the relative contributions from *intra*- and *inter*molecular interactions on actinide redox chemistry, improved predictive capabilities for controlling *f*-element reactivity, and provided a straightforward approach for evaluating the impact of outer-coordination sphere ions on metal electron transfer chemistry. The results demonstrated that both M^{1+} and $X^{1–}$ components of a molten salt can be used to tune and manipulate uranium redox chemistry across substantial potential ranges and supported the initial hypothesis described in the introduction. The results additionally highlighted a powerful approach for controlling uranium redox reactivity in molten salt solutions, given that the identity of the molten salt M^{1+} and $X^{1–}$ ions could be easily and independently changed. We anticipate that this insight will aid researchers, engineers, and technologists working in applied nuclear sectors that utilize molten salt

technologies, particularly in the actinide electrorefining and molten salt nuclear reactor industries. Finally, this approach for characterizing how the outer- and inner-coordination spheres modulate electron transfer chemistry should be transferable to non-actinide analytes (e.g. lanthanides, *d*-block metals, and main group elements) and enable outer- and inner-coordination sphere effects on redox chemistry to be quantitatively evaluated beyond the 5*f*-block metals.

Materials and Methods

General Material Considerations. Potassium chloride (99.99%, anhydrous beads, Millipore Sigma), sodium chloride (99.99%, anhydrous beads, Millipore Sigma), lithium chloride (99.995%, anhydrous beads, BeanTown Chemical), potassium bromide (99.95%, anhydrous, BeanTown Chemical), potassium iodide (99.995%, anhydrous, BeanTown Chemical), nickel(II) chloride (99.9%, anhydrous, BeanTown Chemical), nickel(II) bromide (99%, anhydrous, BeanTown Chemical), nickel(II) iodide (99.5%, anhydrous, BeanTown Chemical), nickel wire (99.995%, 1 mm diameter, BeanTown Chemical), hydrochloric acid (Optima grade, Fisher Scientific), nitric acid (Optima grade, Fisher Scientific), and isopropanol (99.9%, HPLC grade, Sigma-Aldrich) were obtained commercially and used as received.

General Electrochemical Considerations. All voltammetric measurements were conducted in an argon-filled positive pressure VAC Genesis glovebox (<1 ppm O_2 and <1 ppm H_2O) using either a CH Instruments 620C or a BioLogic SP-50e potentiostat. The potentiostat was connected to the cell using feedthroughs in the wall of the glovebox. Glassy carbon rods (3 mm diameter, 20 cm length, Alfa Aesar) and uranium rods (3 mm diameter, 15 cm length, Los Alamos National Laboratory) were used as working and counter electrodes. Mullite tubes (5 mm outer diameter, 3 mm inner diameter, 14 cm length, Anderman Industrial Ceramics) were used as the exterior

housing for each Ni/NiX_2 ($X = Cl^{1-}$, Br^{1-}, I^{1-}) reference electrode. In all cases, quartz tubes (27 mm outer diameter, 25 mm inner diameter, 13.5 cm length, Technical Glass Products, Inc. or Quartz Scientific, Inc.) were used as the electrochemical cells. All electrodes and electrochemical cells were dried in an oven overnight at 200 °C before use. Omitting drying steps or carrying out the experiments in the presence of oxygen, water, or organic solvent vapor resulted black decomposition products accumulating in the molten salt solutions.

Uranium Rod Fabrication. Uranium rods (3 mm diameter) were manufactured from existing depleted uranium plates (12-inch width) that were approximately 3.5 mm thick. Nominal uranium rods were cut from the plates and worked through 3 mm dies in stages from both ends using a Torrington 211 rotary swager. The resulting uranium rods (3 mm diameter) were then sheared to a length of 15 cm.

Molten Salt Furnace Details. All molten salt experiments employed a custom vertical furnace that consisted of two semi-cylindrical ceramic heating elements (ThermCraft RH211, 2 in height, 1.25 in inner diameter, 100 W, 28.5 V) housed inside two semi-cylindrical alumina-based ceramic fiber insulation halves (ThermCraft, 6 in height, 3.125 in thick). The furnace halves were wrapped with ceramic fiber insulation and secured together with hose clamps such that a central hole (1.25 in diameter) was formed on the top of the furnace. The hole extended through the middle of the furnace and stopped 2 inches from the bottom of the insulation. A steel tube liner (10 cm length, 3.1 cm outer diameter) was inserted into the furnace opening to secure electrochemical cells in the center of the heating elements. Furnace power was supplied by a Meanwell 27V DC power supply (ESP-240-27) coupled to an Omega PID controller (CN8DPT-440-DC) via a Crydom

100VDC/60A solid-state relay (D1D60). Overtemperature protection was provided by an Omega limit switch (CN708) connected to an independent thermocouple probe. A schematic of the furnace can be found in the Supporting Information.

Uranium Electrochemistry in Molten Salt Solutions. Electrochemical measurements in molten salt solutions were carried out in an argon-filled glovebox free from contamination with oxygen, moisture, and organic solvents. All electrochemical experiments used a three-electrode setup. Glassy carbon rods were used as the working and counter electrodes for all swept-potential electrochemical measurements. Uranium rods were employed as the working and counter electrodes in all oxidative constant-current experiments to introduce uranium into molten salt solutions. In all experiments, the reference electrode consisted of a clean nickel wire housed in a clean mullite tube that contained a solution of alkali halide salt (LiCl, NaCl, KCl, KBr, or KI) solution containing 1 wt.% NiX_2 ($X = Cl^{1-}$, Br^{1-}, I^{1-}). A new reference electrode was constructed from a clean mullite tube, clean Ni wire, and fresh salt for each experiment to minimize cross-contamination.

Before heating the furnace, the quartz electrochemical cell was filled with alkali halide salt and the electrodes were placed inside. The electrodes were held about 0.5 in apart and immersed the same length into the electrochemical cell. Experiments with LiCl, NaCl, or KCl used 2.5 g (59, 43, or 33 mmol, respectively) of salt. Experiments with KBr or KI used 3.5 g (29 mmol) or 4 g (24 mmol) of salt, respectively. The assembled electrochemical cell was placed in the furnace, the furnace was heated to 850 °C, and the cell was allowed to rest for about 2 hours at 850 °C to give the reference electrode time to equilibrate, as is common in the literature.[1–3] After the equilibration time, cyclic voltammograms were recorded to establish that no redox-active entities were visible

within the molten salt electrochemical window. Subsequently, uranium was introduced into the melt via electrooxidation of uranium metal and electrochemical experiments were performed.

At the end of each experiment, the furnace was powered down and cooled to room temperature. The cell was cooled to room temperature and removed from the glovebox. Water was added and the salts were washed out of the cell. We note that we have not observed any hazardous or reactive uranium compounds to be generated under our experimental conditions. The glassy carbon rods were rinsed with water, polished with an alumina (0.05 μm) slurry in water, soaked in aqua regia (~2 min), and then soaked in concentrated aqueous HCl solution for 2 to 6 hours. The uranium rods were washed with water to remove excess salt, soaked in 50% aqueous nitric acid (~5 min) to remove any adhered uranium oxides, then sequentially washed with water and isopropanol, dried, and returned to the glovebox. The reference electrode was disassembled, and the nickel wire was rinsed and soaked in water to remove salt deposits. The mullite tube was thoroughly washed with water and soaked in aqua regia for 12 to 24 hours. Afterwards, the inside of the mullite tube was rinsed again with water and filled with concentrated HCl. The tube was then placed in a solution of HCl to soak for 12 hours.

Electrochemical Generation of Uranium-Containing Molten Salt Solutions. After determining the electrochemical window and verifying that extraneous redox-active species were not present, uranium was introduced into each molten salt via oxidative dissolution. The two glassy carbon rods were replaced with two uranium metal rods as the working and counter electrodes. Uranium ions were stripped from the metal working electrode into the molten salt solution by applying a potential to achieve −100 mA of current. The initial potentials required were −1.2 V in LiCl and KCl, −1.1 V in NaCl, −1.0 V in KBr, and −0.9 V in KI. After sufficient charge had been

passed to generate a uranium (0.04–0.76 wt.% U^{III}) molten salt solution, the uranium rods were replaced by the glassy carbon working and counter electrodes, and electrochemistry experiments were performed.

Uranium Digestion and ICP-AES Stable Element Quantification. The following procedure was modified from reported methods used to digest thorium oxide samples.[4] To digest uranium samples for ICP analysis, molten salt samples were dissolved in Milli-Q water (20 mL) inside the quartz cell. The supernatant was decanted to remove as much salt as possible, leaving behind uranium residues as well as some adhered to the side of the cell. Once the salt was removed, the cell was scored, broken, and the quartz fragments were placed into a quartz beaker containing a Teflon stir bar. The quartz fragments were submerged in HNO_3 (6.5 M) solution containing HF (20 mL, 5 mM). A watch glass was used to seal the top of the beaker, and the solution was then heated to 150 °C and stirred at 500 rpm for 1 hr. After 1 hr, no traces of uranium were observed on the quartz shards, and the solutions were cooled to room temperature then stored in a Nalgene container.

Stable element concentrations for uranium were quantified by inductively coupled plasma-atomic emission spectroscopy (ICP-AES) utilizing a PerkinElmer Optima 8000 instrument. Limit of Quantification (LOQ) and Limit of Detection (LOD) for uranium were determined following an established procedure.[5] Manganese was utilized as an internal calibration standard for emissions. Uranium calibration standards were prepared gravimetrically using a 10000 ppm [U] HNO_3 (0.1 M) standard by Inorganic Ventures. A five-point calibration curve was made, from 25 ppm to 1000 ppm for uranium in HNO_3 (0.1 M). The solutions from the separate digestions were prepared gravimetrically to an estimated 500 ppm, calculated from an assumed 100% faradaic efficiency during the anodic chronopotentiometry uranium rod experiments. Raw counts given in

ppm were then back calculated to determine the weight % of uranium in the melts from the starting salt masses. Faradaic efficiencies were extrapolated from the anticipated ppm versus observed ppm of uranium after analysis and correlated with the charged passed during chronopotentiometry.

Associated Content

Supporting Information

The Supporting Information is available free of charge at https://pubs.acs.org/doi/10.XXXX/jacs.XXXXXXX.

Full experimental details, a full description of the approach for referencing electrochemical potentials, and additional discussion of the Coulombic model are given in the Supporting Information (PDF).

Author Information

Corresponding Authors

Nickolas H. Anderson – Los Alamos National Laboratory, Los Alamos, New Mexico 87545, United States; orcid.org/0000-0003-1016-3420; Email: nhanderson@lanl.gov

Stosh A. Kozimor – Los Alamos National Laboratory, Los Alamos, New Mexico 87545, United States; orcid.org/0000-0001-7387-0507; Email: stosh@lanl.gov

Authors

Travis Marshall-Roth – Los Alamos National Laboratory, Los Alamos, New Mexico 87545, United States; orcid.org/0000-0002-6245-6404

Molly M. MacInnes – Los Alamos National Laboratory, Los Alamos, New Mexico 87545, United States; orcid.org/0000-0001-9513-7402

Aldo M. Jordan – Los Alamos National Laboratory, Los Alamos, New Mexico 87545, United States

Ida D. Piedmonte – Los Alamos National Laboratory, Los Alamos, New Mexico 87545, United States; orcid.org/0000-0003-3440-7856

Kristen A. Pace – Los Alamos National Laboratory, Los Alamos, New Mexico 87545, United States; orcid.org/0000-0001-8574-8939

Sara L. Adelman – Los Alamos National Laboratory, Los Alamos, New Mexico 87545, United States; orcid.org/0000-0001-7989-3451

Jason C. Cooley – Los Alamos National Laboratory, Los Alamos, New Mexico 87545, United States; orcid.org/0000-0002-2649-2352

Monica S. Mullis – Los Alamos National Laboratory, Los Alamos, New Mexico 87545, United States

Veronika Mocko – Los Alamos National Laboratory, Los Alamos, New Mexico 87545, United States; orcid.org/0000-0001-6041-6778

Francisca R. Rocha – Los Alamos National Laboratory, Los Alamos, New Mexico 87545, United States

Benjamin W. Stein – Los Alamos National Laboratory, Los Alamos, New Mexico 87545, United States

Complete contact information is available at:

https://pubs.acs.org/10.XXXX/jacs.XXXXXXX

Notes

The authors declare no competing financial interest. LA-UR-25-29884.

Acknowledgments

We thank the U.S. Department of Energy, Office of Science, Office of Basic Energy Sciences, Heavy Element Chemistry program (2020LANLE372) and LANL's Laboratory Directed Research and Development program (20190364ER and 20220054DR). Additional support was provided by U.S. DOE, National Nuclear Security Association (NNSA), Plutonium Modernization Program (NA-91). Postdoctoral support was provided in part by the Los Alamos National Laboratory Named Glenn T. Seaborg Institute (T.M.-R.) and the Agnew (I.D.P.) Postdoctoral Fellowships. LANL is an affirmative action and equal opportunity employer managed by Triad National Security, LLC, for the NNSA of the U.S. DOE.

References

(1) Steed, J. W. First- and Second-Sphere Coordination Chemistry of Alkali Metal Crown Ether Complexes. *Coord. Chem. Rev.* **2001**, *215* (1), 171–221. https://doi.org/10.1016/S0010-8545(01)00317-4.

(2) Oyama, D.; Abe, R.; Takase, T. Coordination Chemistry of Mononuclear Ruthenium Complexes Bearing Versatile 1,8-Naphthyridine Units: Utilization of Specific Reaction Sites Constructed by the Secondary Coordination Sphere. *Coord. Chem. Rev.* **2018**, *375*, 424–433. https://doi.org/10.1016/j.ccr.2017.11.024.

(3) Oktawiec, J.; Jiang, H. Z. H.; Turkiewicz, A. B.; Long, J. R. Influence of the Primary and Secondary Coordination Spheres on Nitric Oxide Adsorption and Reactivity in Cobalt(II)–Triazolate Frameworks. *Chem. Sci.* **2021**, *12* (43), 14590–14598. https://doi.org/10.1039/D1SC03994F.

(4) Jones, J. R.; Ziller, J. W.; Borovik, A. S. Modulating the Primary and Secondary Coordination Spheres within a Series of Co^{II} —OH Complexes. *Inorg. Chem.* **2017**, *56* (3), 1112–1120. https://doi.org/10.1021/acs.inorgchem.6b01956.

(5) Rakowski DuBois, M.; DuBois, D. L. The Roles of the First and Second Coordination Spheres in the Design of Molecular Catalysts for H_2 Production and Oxidation. *Chem. Soc. Rev.* **2009**, *38* (1), 62–72. https://doi.org/10.1039/B801197B.

(6) Wang, Z.; Xu, R.; Ye, Q.; Jin, X.; Lu, Z.; Yang, Z.; Wang, Y.; Yan, T.; Liu, Y.; Pan, Z.; Hwang, S.; Fan, H. J. Tailoring First Coordination Sphere of Dual-Metal Atom Sites Boosts Oxygen Reduction and Evolution Activities. *Adv. Funct. Mater.* **2024**, *34* (28), 2315376. https://doi.org/10.1002/adfm.202315376.

(7) Yang, G.; Wang, D.; Wang, Y.; Hu, W.; Hu, S.; Jiang, J.; Huang, J.; Jiang, H.-L. Modulating the Primary and Secondary Coordination Spheres of Single Ni(II) Sites in Metal–Organic Frameworks for Boosting Photocatalysis. *J. Am. Chem. Soc.* **2024**, *146* (15), 10798–10805. https://doi.org/10.1021/jacs.4c00972.

(8) Forgan, R. S.; Roach, B. D.; Wood, P. A.; White, F. J.; Campbell, J.; Henderson, D. K.; Kamenetzky, E.; McAllister, F. E.; Parsons, S.; Pidcock, E.; Richardson, P.; Swart, R. M.; Tasker, P. A. Using the Outer Coordination Sphere to Tune the Strength of Metal Extractants. *Inorg. Chem.* **2011**, *50* (10), 4515–4522. https://doi.org/10.1021/ic200154y.

(9) Dalrymple, S. A.; Shimizu, G. K. H. Exploiting Complementary Second-Sphere Effects in Supramolecular Coordination Solids. *Supramol. Chem.* **2003**, *15* (7–8), 591–606. https://doi.org/10.1080/10610270310001605188.

(10) Lakshmi, B.; Samuelson, A. G.; Jovan Jose, K. V.; Gadre, S. R.; Arunan, E. Is There a Hydrogen Bond Radius? Evidence from Microwave Spectroscopy, Neutron Scattering and X-Ray Diffraction Results. *New J. Chem.* **2005**, *29* (2), 371. https://doi.org/10.1039/b411815d.

(11) Oksanen, E.; Chen, J. C.-H.; Fisher, S. Z. Neutron Crystallography for the Study of Hydrogen Bonds in Macromolecules. *Molecules* **2017**, *22* (4), 596. https://doi.org/10.3390/molecules22040596.

(12) Duan, W.-L.; Wang, H.-C.; Martí-Rujas, J.; Guo, F. Fluorescence-Based Detection of Nitroaromatics Using a Luminescent Second Sphere Adduct Self-Assembled by Charge-Assisted Hydrogen Bonds. *CrystEngComm* **2018**, *20* (3), 323–327. https://doi.org/10.1039/C7CE01743J.

(13) Oktawiec, J.; Jiang, H. Z. H.; Vitillo, J. G.; Reed, D. A.; Darago, L. E.; Trump, B. A.; Bernales, V.; Li, H.; Colwell, K. A.; Furukawa, H.; Brown, C. M.; Gagliardi, L.; Long, J. R. Negative Cooperativity upon Hydrogen Bond-Stabilized O_2 Adsorption in a Redox-Active Metal–Organic Framework. *Nat. Commun.* **2020**, *11* (1), 3087. https://doi.org/10.1038/s41467-020-16897-z.

(14) Rhoda, H. M.; Heyer, A. J.; Snyder, B. E. R.; Plessers, D.; Bols, M. L.; Schoonheydt, R. A.; Sels, B. F.; Solomon, E. I. Second-Sphere Lattice Effects in Copper and Iron Zeolite Catalysis. *Chem. Rev.* **2022**, *122* (14), 12207–12243. https://doi.org/10.1021/acs.chemrev.1c00915.

(15) Trouvé, J.; Gramage-Doria, R. Beyond Hydrogen Bonding: Recent Trends of Outer Sphere Interactions in Transition Metal Catalysis. *Chem. Soc. Rev.* **2021**, *50* (5), 3565–3584. https://doi.org/10.1039/D0CS01339K.

(16) Kumar, A.; Lionetti, D.; Day, V. W.; Blakemore, J. D. Redox-Inactive Metal Cations Modulate the Reduction Potential of the Uranyl Ion in Macrocyclic Complexes. *J. Am. Chem. Soc.* **2020**, *142* (6), 3032–3041. https://doi.org/10.1021/jacs.9b11903.

(17) Haaf, S.; Kaifer, E.; Wadepohl, H.; Himmel, H. Use of Crown Ether Functions as Secondary Coordination Spheres for the Manipulation of Ligand–Metal Intramolecular Electron Transfer in Copper–Guanidine Complexes. *Chem. Eur. J.* **2021**, *27* (3), 959–970. https://doi.org/10.1002/chem.202003469.

(18) Sahu, S.; Widger, L. R.; Quesne, M. G.; De Visser, S. P.; Matsumura, H.; Moënne-Loccoz, P.; Siegler, M. A.; Goldberg, D. P. Secondary Coordination Sphere Influence on the Reactivity of Nonheme Iron(II) Complexes: An Experimental and DFT Approach. *J. Am. Chem. Soc.* **2013**, *135* (29), 10590–10593. https://doi.org/10.1021/ja402688t.

(19) Hall, J. N.; Vicchio, S. P.; Kropf, A. J.; Delferro, M.; Bollini, P. Can the Rate of a Catalytic Turnover Be Altered by Ligands in the Absence of Direct Binding Interactions? *J. Am. Chem. Soc.* **2024**, *146* (17), 12113–12129. https://doi.org/10.1021/jacs.4c01978.

(20) Pramanik, S.; Li, B.; Driscoll, D. M.; Johnson, K. R.; Evans, B. R.; Damron, J. T.; Ivanov, A. S.; Jiang, D.; Einkauf, J.; Popovs, I.; Jansone-Popova, S. Tetradentate Ligand's Chameleon-Like Behavior Offers Recognition of Specific Lanthanides. *J. Am. Chem. Soc.* **2024**, *146* (37), 25669–25679. https://doi.org/10.1021/jacs.4c07332.

(21) Brigham, D. M.; Ivanov, A. S.; Moyer, B. A.; Delmau, L. H.; Bryantsev, V. S.; Ellis, R. J. Trefoil-Shaped Outer-Sphere Ion Clusters Mediate Lanthanide(III) Ion Transport with Diglycolamide Ligands. *J. Am. Chem. Soc.* **2017**, *139* (48), 17350–17358. https://doi.org/10.1021/jacs.7b07318.

(22) Driscoll, D. M.; Liu, H.; Reinhart, B.; Popovs, I.; Bocharova, V.; Jansone-Popova, S.; Jiang, D.; Ivanov, A. S. Noncoordinating Secondary Sphere Ion Modulates Supramolecular Clustering of Lanthanides. *J. Phys. Chem. Lett.* **2022**, *13* (51), 12076–12081. https://doi.org/10.1021/acs.jpclett.2c03423.

(23) Creutz, S. E.; Peters, J. C. Exploring Secondary-Sphere Interactions in Fe–N_xH_y Complexes Relevant to N_2 Fixation. *Chem. Sci.* **2017**, *8* (3), 2321–2328. https://doi.org/10.1039/C6SC04805F.

(24) Zhao, M.; Wang, H.-B.; Ji, L.-N.; Mao, Z.-W. Insights into Metalloenzyme Microenvironments: Biomimetic Metal Complexes with a Functional Second Coordination Sphere. *Chem. Soc. Rev.* **2013**, *42* (21), 8360–8375. https://doi.org/10.1039/c3cs60162e.

(25) Drover, M. W. A Guide to Secondary Coordination Sphere Editing. *Chem. Soc. Rev.* **2022**, *51* (6), 1861–1880. https://doi.org/10.1039/D2CS00022A.

(26) Jeong, W. J.; Lee, J.; Eom, H.; Song, W. J. A Specific Guide for Metalloenzyme Designers: Introduction and Evolution of Metal-Coordination Spheres Embedded in Protein Environments. *Acc. Chem. Res.* **2023**, *56* (18), 2416–2425. https://doi.org/10.1021/acs.accounts.3c00336.

(27) Van Stappen, C.; Dai, H.; Jose, A.; Tian, S.; Solomon, E. I.; Lu, Y. Primary and Secondary Coordination Sphere Effects on the Structure and Function of *S* -Nitrosylating Azurin. *J. Am. Chem. Soc.* **2023**, *145* (37), 20610–20623. https://doi.org/10.1021/jacs.3c07399.

(28) Ginovska-Pangovska, B.; Dutta, A.; Reback, M. L.; Linehan, J. C.; Shaw, W. J. Beyond the Active Site: The Impact of the Outer Coordination Sphere on Electrocatalysts for Hydrogen Production and Oxidation. *Acc. Chem. Res.* **2014**, *47* (8), 2621–2630. https://doi.org/10.1021/ar5001742.

(29) Baldwin, A. G.; Ivanov, A. S.; Williams, N. J.; Ellis, R. J.; Moyer, B. A.; Bryantsev, V. S.; Shafer, J. C. Outer-Sphere Water Clusters Tune the Lanthanide Selectivity of Diglycolamides. *ACS Cent. Sci.* **2018**, *4* (6), 739–747. https://doi.org/10.1021/acscentsci.8b00223.

(30) Roy, S.; Liu, Y.; Topsakal, M.; Dias, E.; Gakhar, R.; Phillips, W. C.; Wishart, J. F.; Leshchev, D.; Halstenberg, P.; Dai, S.; Gill, S. K.; Frenkel, A. I.; Bryantsev, V. S. A Holistic Approach for Elucidating Local Structure, Dynamics, and Speciation in Molten Salts with High Structural Disorder. *J. Am. Chem. Soc.* **2021**, *143* (37), 15298–15308. https://doi.org/10.1021/jacs.1c06742.

(31) Zheng, K.; Marcella, N.; Smith, A. L.; Frenkel, A. I. Decoding the Pair Distribution Function of Uranium in Molten Fluoride Salts from X-Ray Absorption Spectroscopy Data

by Machine Learning. *J. Phys. Chem. C* **2024**, *128* (18), 7635–7642. https://doi.org/10.1021/acs.jpcc.4c01898.

(32) Inman, D.; Hills, G. J.; Young, L.; Bockris, J. O. Electrode Reactions in Molten Salts: The Uranium + Uranium Trichloride System. *Trans. Faraday Soc.* **1959**, *55*, 1904. https://doi.org/10.1039/tf9595501904.

(33) Hill, D. L.; Perano, J.; Osteryoung, R. A. An Electrochemical Study of Uranium in Fused Chlorides. *J. Electrochem. Soc.* **1960**, *107* (8), 698. https://doi.org/10.1149/1.2427811.

(34) Inman, D.; Bockris, J. O. The Reversible Electrode Potential of the System U/UCl_3 in Molten Chloride Solvents. *Can. J. Chem.* **1961**, *39* (5), 1161–1163. https://doi.org/10.1139/v61-146.

(35) Lambert, H.; Kerry, T.; Sharrad, C. A. Preparation of Uranium(III) in a Molten Chloride Salt: A Redox Mechanistic Study. *J. Radioanal. Nucl. Chem.* **2018**, *317* (2), 925–932. https://doi.org/10.1007/s10967-018-5953-7.

(36) Li, B.; Dai, S.; Jiang, D. First-Principles Molecular Dynamics Simulations of UCl_n –NaCl (n = 3, 4) Molten Salts. *ACS Appl. Energy Mater.* **2019**, *2* (3), 2122–2128. https://doi.org/10.1021/acsaem.8b02157.

(37) MacInnes, M. M.; Jones, Z. R.; Li, B.; Anderson, N. H.; Batista, E. R.; DiMucci, I. M.; Eiroa-Lledo, C.; Knope, K. E.; Livshits, M. Y.; Kozimor, S. A.; Mocko, V.; Pace, K. A.; Rocha, F. R.; Stein, B. W.; Wacker, J. N.; Yang, P. Using Molten Salts to Probe Outer-Coordination Sphere Effects on Lanthanide(III)/(II) Electron-Transfer Reactions. *Dalton Trans.* **2021**, *50* (43), 15696–15710. https://doi.org/10.1039/D1DT02708E.

(38) Lee, C. H.; Kim, T.-J.; Yoon, D.; Jang, J.; Kim, G.-Y.; Lee, S.-J. Efficient Preparation of UCl_3 by $ZnCl_2$ Mediated Chlorination. *J. Radioanal. Nucl. Chem.* **2019**, *322* (2), 331–336. https://doi.org/10.1007/s10967-019-06782-5.

(39) Yoon, D.; Paek, S.; Lee, C. Chlorination of Uranium Metal to Uranium Trichloride Using Ammonium Chloride. *J. Radioanal. Nucl. Chem.* **2022**, *331* (5), 2209–2216. https://doi.org/10.1007/s10967-022-08285-2.

(40) Chamberlain, J.; Simpson, M. F. Development of a Scalable Method to Chlorinate UO_2 to UCl_3 Using $ZrCl_4$. *J. Radioanal. Nucl. Chem.* **2022**, *331* (12), 4983–4996. https://doi.org/10.1007/s10967-022-08473-0.

(41) Rudel, S. S.; Kraus, F. Facile Syntheses of Pure Uranium Halides: UCl_4, UBr_4 and UI_4. *Dalton Trans.* **2017**, *46* (18), 5835–5842. https://doi.org/10.1039/C7DT00726D.

(42) Singh, V.; Bruneau, C.; Karmiol, Z.; Moon, J.; Chidambaram, D. The Effect of Oxychloride Formation on the Electroanalytical Determination of Chlorides in Molten Salts: An Investigation of SmOCl in Molten LiCl–KCl. *J. Radioanal. Nucl. Chem.* **2023**, *332* (3), 691–697. https://doi.org/10.1007/s10967-023-08800-z.

(43) Prabhakara Reddy, B.; Vandarkuzhali, S.; Subramanian, T.; Venkatesh, P. Electrochemical Studies on the Redox Mechanism of Uranium Chloride in Molten LiCl–KCl Eutectic. *Electrochim. Acta* **2004**, *49* (15), 2471–2478. https://doi.org/10.1016/j.electacta.2004.02.002.

(44) Shirai, O.; Iwai, T.; Suzuki, Y.; Sakamura, Y.; Tanaka, H. Electrochemical Behavior of Actinide Ions in LiCl–KCl Eutectic Melts. *J. Alloys Compd.* **1998**, *271–273*, 685–688. https://doi.org/10.1016/S0925-8388(98)00187-X.

(45) Janz, G. J. *Thermodynamic and Transport Properties for Molten Salts: Correlation Equations for Critically Evaluated Density, Surface Tension, Electrical Conductance, and Viscosity Data*; Journal of physical and chemical reference data Supplement; American Institute of Physics: New York, NY, 1988.

(46) Bartels, R. A.; Smith, P. A. Pressure and Temperature Dependence of the Static Dielectric Constants of KCl, NaCl, LiF, and MgO. *Phys. Rev. B* **1973**, *7* (8), 3885–3892. https://doi.org/10.1103/PhysRevB.7.3885.

(47) Cassayre, L.; Caravaca, C.; Jardin, R.; Malmbeck, R.; Masset, P.; Mendes, E.; Serp, J.; Soucek, P.; Glatz, J.-P. On the Formation of U–Al Alloys in the Molten LiCl–KCl Eutectic. *Journal of Nuclear Materials* **2008**, *378* (1), 79–85. https://doi.org/10.1016/j.jnucmat.2008.05.004.

(48) Serrano, K.; Taxil, P.; Dugne, O.; Bouvet, S.; Puech, E. Preparation of Uranium by Electrolysis in Chloride Melt. *J. Nucl. Mater.* **2000**, *282* (2–3), 137–145. https://doi.org/10.1016/S0022-3115(00)00423-2.

(49) Kuznetsov, S. A.; Hayashi, H.; Minato, K.; Gaune-Escard, M. Electrochemical Transient Techniques for Determination of Uranium and Rare-Earth Metal Separation Coefficients in Molten Salts. *Electrochim. Acta* **2006**, *51* (12), 2463–2470. https://doi.org/10.1016/j.electacta.2005.07.028.

(50) Gaur, H. C.; Jindal, H. L. Standard Electrode Potentials in Molten Chlorides. *Electrochim. Acta* **1968**, *13* (4), 835–842. https://doi.org/10.1016/0013-4686(68)85016-9.

(51) Berghoute, Y.; Salmi, A.; Lantelme, F. Internal Reference Systems for Fused Electrolytes. *J. Electroanal. Chem.* **1994**, *365* (1–2), 171–177. https://doi.org/10.1016/0022-0728(93)01972-D.

(52) Snook, G. A.; Best, A. S.; Pandolfo, A. G.; Hollenkamp, A. F. Evaluation of a Ag|Ag+ Reference Electrode for Use in Room Temperature Ionic Liquids. *Electrochem. Commun.* **2006**, *8* (9), 1405–1411. https://doi.org/10.1016/j.elecom.2006.07.004.

(53) Bhatt, A. I.; Snook, G. A. Reference Electrodes for Ionic Liquids and Molten Salts. In *Handbook of Reference Electrodes*; Inzelt, G., Lewenstam, A., Scholz, F., Eds.; Springer Berlin Heidelberg: Berlin, Heidelberg, 2013; pp 189–227. https://doi.org/10.1007/978-3-642-36188-3_7.

(54) Fitzhugh, R. L.; Clark, A. D.; Nickerson, S. D.; Memmott, M. J.; Harb, J. N. On the Electrochemical Thermodynamics of Minor Components in Molten Salt Mixtures. *J. Electrochem. Soc.* **2021**, *168* (2), 026502. https://doi.org/10.1149/1945-7111/abdd7c.

(55) Lhermitte, C. R.; Parker, S. S.; Jackson, J. M.; Monreal, M. J. Communication—$Mg^{2+/0}$ as a Reliable Reference Electrode for Molten Chloride Salts. *J. Electrochem. Soc.* **2021**, *168* (6), 066501. https://doi.org/10.1149/1945-7111/ac0303.

(56) Dale, O. R.; Felling, F.; Gonzalez, M.; Zhang, C.; Simpson, M. F. Ni/NiO Reference Electrode Potential Measurements in Molten $CaCl_2$–CaO. *J. Electrochem. Soc.* **2023**, *170* (6), 066509. https://doi.org/10.1149/1945-7111/acdd25.

(57) Torrie, J. M.; Fuller, R.; Rappleye, D. Communication—The Development of a Stable and Practical Saturated Reference Electrode for Molten Chloride Salt Systems. *J. Electrochem. Soc.* **2024**, *171* (5), 053508. https://doi.org/10.1149/1945-7111/ad4c0c.

(58) Mejia, C.; Christensen, N.; Ceron, R. R.; Rappleye, D. Development of a Stable and Buffered Reference Electrode for Binary Molten Chlorides Salts. *Electrochim. Acta* **2025**, *512*, 145496. https://doi.org/10.1016/j.electacta.2024.145496.

(59) Rappleye, D. S.; Fuller, R. G. Bringing the Analysis of Electrodeposition Signals in Voltammetry Out of the Shadows. *J. Electrochem. Soc.* **2023**, *170* (6), 063505. https://doi.org/10.1149/1945-7111/acd879.

(60) Krulic, D.; Fatouros, N.; Liu, D. A Complementary Survey of Staircase Voltammetry with Metal Ion Deposition on Macroelectrodes. *J. Electroanal. Chem.* **2015**, *754*, 30–39. https://doi.org/10.1016/j.jelechem.2015.06.012.

(61) Fatouros, N.; Krulic, D.; Groult, H. Linear Sweep and Staircase Voltammetries for Reversible Deposition of Metal Ions on the Same Metal and on Foreign Substrates. *J. Electroanal. Chem.* **2009**, *625* (1), 1–6. https://doi.org/10.1016/j.jelechem.2008.07.028.

(62) Notz, K.; Keenan, A. G. Cation Selectivity of Pyrex Glass Electrode in Fused Ammonium Nitrate. *J. Phys. Chem.* **1966**, *70* (3), 662–666. https://doi.org/10.1021/j100875a010.

(63) Stern, K. H. Membrane Potentials and Ion Selectivity of Fused Silica in Molten Salts. *J. Phys. Chem.* **1968**, *72* (6), 1963–1975. https://doi.org/10.1021/j100852a019.

(64) Stull, D. R.; Prophet, H. *JANAF Thermochemical Tables, Second Edition*, 0 ed.; NBS NSRDS 37; National Bureau of Standards: Gaithersburg, MD, 1971; p NBS NSRDS 37. https://doi.org/10.6028/NBS.NSRDS.37.

(65) Aoki, K.; Honda, K.; Tokuda, K.; Matsuda, H. Voltammetry at Microcylinder Electrodes. *J. Electroanal. Chem.* **1985**, *182* (2), 267–279. https://doi.org/10.1016/0368-1874(85)87005-2.

(66) Kim, C. M.; Yoon, S. P.; Cho, S. K. Determination of Diffusion Coefficient in High Temperature Molten Salt Using Cyclic Voltammetry on Microwire Electrode: Its Validity and Limitation. *J. Electroanal. Chem.* **2021**, *894*, 115353. https://doi.org/10.1016/j.jelechem.2021.115353.

(67) Compton, R. G.; Banks, C. E. *Understanding Voltammetry (Third Edition)*; World Scientific, 2018.

(68) Nasch, P. M.; Steinemann, S. G. Density and Thermal Expansion of Molten Manganese, Iron, Nickel, Copper, Aluminum and Tin by Means of the Gamma-Ray Attenuation Technique. *Phys. Chem. Liq.* **1995**, *29* (1), 43–58. https://doi.org/10.1080/00319109508030263.

(69) Tylka, M. M.; Willit, J. L.; Prakash, J.; Williamson, M. A. Method Development for Quantitative Analysis of Actinides in Molten Salts. *J. Electrochem. Soc.* **2015**, *162* (9), H625–H633. https://doi.org/10.1149/2.0401509jes.

(70) Gao, F.; Wang, C.; Liu, L.; Guo, J.; Chang, S.; Chang, L.; Li, R.; Ouyang, Y. Electrode Processes of Uranium Ions and Electrodeposition of Uranium in Molten LiCl-KCl. *J. Radioanal. Nucl. Chem.* **2009**, *280* (1), 207–218. https://doi.org/10.1007/s10967-008-7417-y.

(71) Tylka, M. M.; Willit, J. L.; Williamson, M. A. Electrochemical Nucleation and Growth of Uranium and Plutonium from Molten Salts. *J. Electrochem. Soc.* **2017**, *164* (8), H5327–H5335. https://doi.org/10.1149/2.0471708jes.

(72) Masset, P.; Bottomley, D.; Konings, R.; Malmbeck, R.; Rodrigues, A.; Serp, J.; Glatz, J.-P. Electrochemistry of Uranium in Molten LiCl-KCl Eutectic. *J. Electrochem. Soc.* **2005**, *152* (6), A1109. https://doi.org/10.1149/1.1901083.

(73) Tasidou, K. A.; Chliatzou, Ch. D.; Assael, M. J.; Antoniadis, K. D.; Mylona, S. K.; Huber, M. L.; Wakeham, W. A. Reference Correlations for the Viscosity of 13 Inorganic Molten Salts. *J. Phys. Chem. Ref. Data* **2019**, *48* (1), 013101. https://doi.org/10.1063/1.5091511.

(74) González-Jiménez, M.; Liao, Z.; Williams, E. L.; Wynne, K. Lifting Hofmeister's Curse: Impact of Cations on Diffusion, Hydrogen Bonding, and Clustering of Water. *J. Am. Chem. Soc.* **2024**, *146* (1), 368–376. https://doi.org/10.1021/jacs.3c09421.

(75) Shannon, R. D. Revised Effective Ionic Radii and Systematic Studies of Interatomic Distances in Halides and Chalcogenides. *Acta Cryst. A* **1976**, *32* (5), 751–767. https://doi.org/10.1107/S0567739476001551.

(76) Brooker, M. H.; Bredig, Max. A. Significance of Both Polarizability and Polarizing Power of Cations in Nitrate Vibrational Spectra. *J. Chem. Phys.* **1973**, *58* (12), 5319–5321. https://doi.org/10.1063/1.1679146.

(77) Grégoire, B.; Ruby, C.; Carteret, C. Structural Cohesion of M^{II} -M^{III} Layered Double Hydroxides Crystals: Electrostatic Forces and Cationic Polarizing Power. *Cryst. Growth Des.* **2012**, *12* (9), 4324–4333. https://doi.org/10.1021/cg3006053.

(78) Song, J.; Wang, Q.; Kang, M.; Jiao, S.; Zhu, H. The Equilibrium between Titanium Ions and Metallic Titanium in the Molten Binary Mixtures of LiCl. *Electrochemistry* **2014**, *82* (12), 1047–1051. https://doi.org/10.5796/electrochemistry.82.1047.

(79) Li, B.; Jones, Z. R.; Eiroa-Lledo, C.; Knope, K. E.; Mocko, V.; Stein, B. W.; Wacker, J. N.; Kozimor, S. A.; Batista, E. R.; Yang, P. Structure and Dynamics of NaCl/KCl/$CaCl_2$ –$EuCl_n$ (n = 2, 3) Molten Salts. *Inorg. Chem.* **2023**, *62* (27), 10528–10538. https://doi.org/10.1021/acs.inorgchem.2c03982.

(80) Duffy, J. A.; Ingram, M. D. Establishment of an Optical Scale for Lewis Basicity in Inorganic Oxyacids, Molten Salts, and Glasses. *J. Am. Chem. Soc.* **1971**, *93* (24), 6448–6454. https://doi.org/10.1021/ja00753a019.

(81) Kłos, J.; Lamperski, S. Analysis of Electrical Double Layer Structure in Molten Salts. *J. Chem. Phys.* **2019**, *150* (6), 064704. https://doi.org/10.1063/1.5082561.

(82) Hazebroucq, S.; Picard, G. S.; Adamo, C. A Theoretical Investigation of Gadolinium (III) Solvation in Molten Salts. *J. Chem. Phys.* **2005**, *122* (22), 224512. https://doi.org/10.1063/1.1931648.

(83) Maltsev, D. S.; Driscoll, D. M.; Zhang, Y.; Neuefeind, J. C.; Reinhart, B.; Agca, C.; Ray, D.; Halstenberg, P. W.; Aziziha, M.; Schorne-Pinto, J.; Besmann, T. M.; Bryantsev, V. S.; Dai, S.; Roy, S.; Ivanov, A. S. Transient Covalency in Molten Uranium(III) Chloride. *J. Am. Chem. Soc.* **2024**, *146* (31), 21220–21224. https://doi.org/10.1021/jacs.4c05765.

(84) Porter, T.; Vaka, M. M.; Steenblik, P.; Della Corte, D. Computational Methods to Simulate Molten Salt Thermophysical Properties. *Commun. Chem.* **2022**, *5* (1), 69. https://doi.org/10.1038/s42004-022-00684-6.

(85) Carmichael, C. D.; Jones, N. A.; Arnold, P. L. Low-Valent Uranium Iodides: Straightforward Solution Syntheses of UI_3 and UI_4 Etherates. *Inorg. Chem.* **2008**, *47* (19), 8577–8579. https://doi.org/10.1021/ic801138e.

Figures, Schemes, and Tables

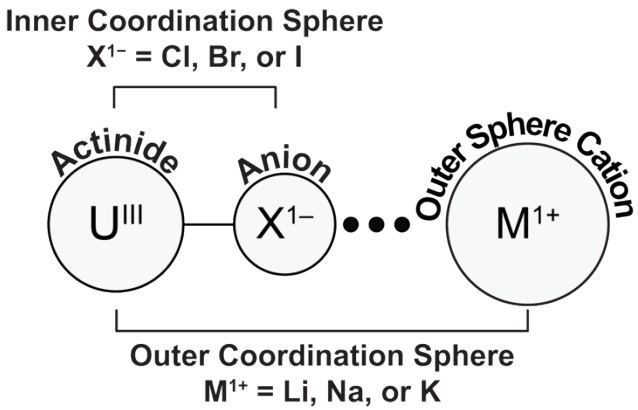

Scheme 1. Idealized interactions of U^{III} with molten salt solutions involving contributions from X^{1-} molten salt anions in the inner coordination sphere and M^{1+} molten salt cations in the outer coordination sphere.

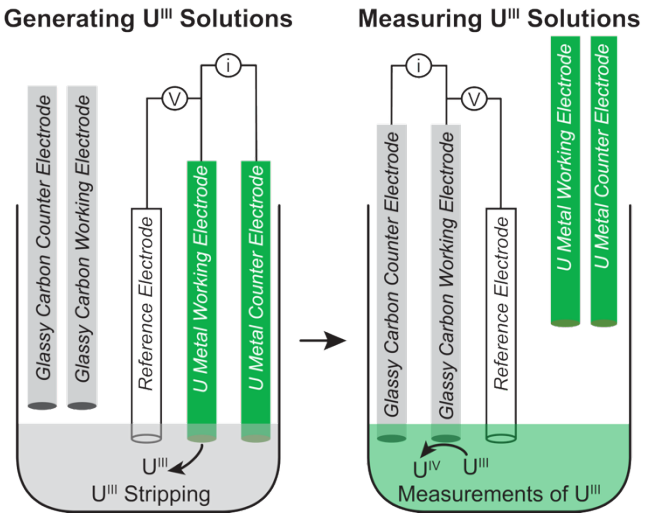

Scheme 2. Generation of U^{III}-containing solutions in molten salts using U^0_{metal} rods (left). Measurement of soluble uranium species in molten salt solutions (right). "V" represents the voltage difference measured by the potentiostat between the working and reference electrodes and "i" is the current measured between the working and counter electrodes.

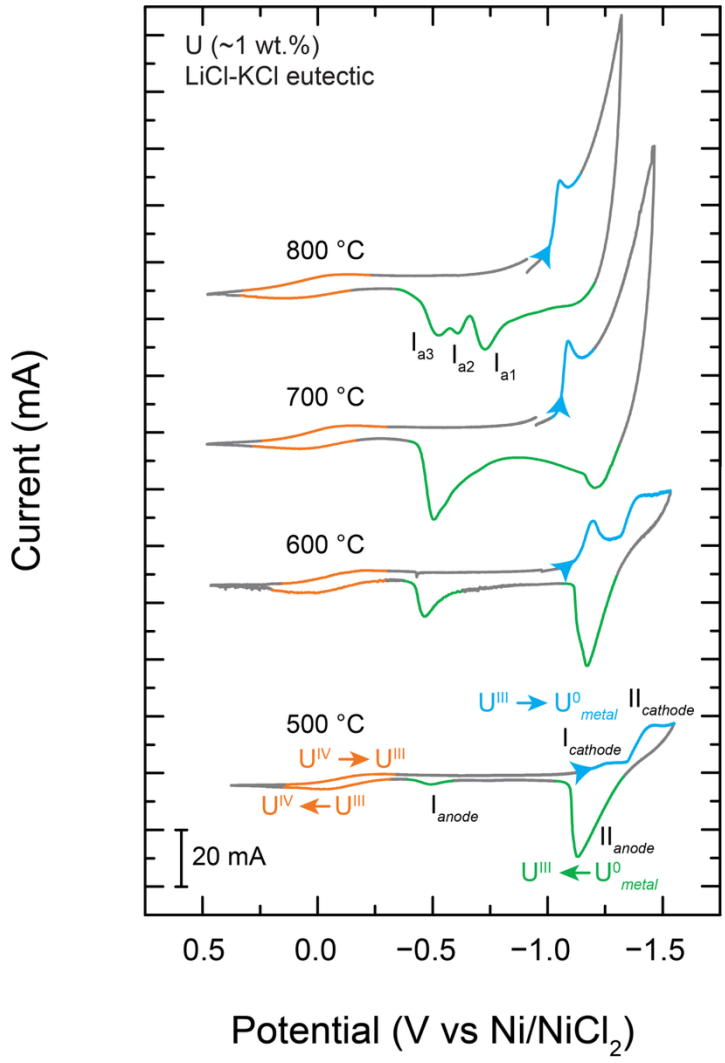

Figure 1. Representative high-temperature cyclic voltammograms of uranium dissolved in LiCl–KCl eutectic (46 wt.% LiCl to 54 wt.% KCl) over a temperature range of 500 to 800 °C. Features attributed to $U^{IV/III}$ (orange), U^{0}_{metal} deposition (blue; $I_{cathode}$ and $II_{cathode}$), and stripping (green; I_{anode}, II_{anode}, I_{a1}, I_{a2}, and I_{a3}) redox processes were labeled accordingly. Data were recorded at a scan rate of 100 mV s^{-1} and referenced to the reference $Ni^{II/0}$ redox reaction in the LiCl–KCl eutectic.

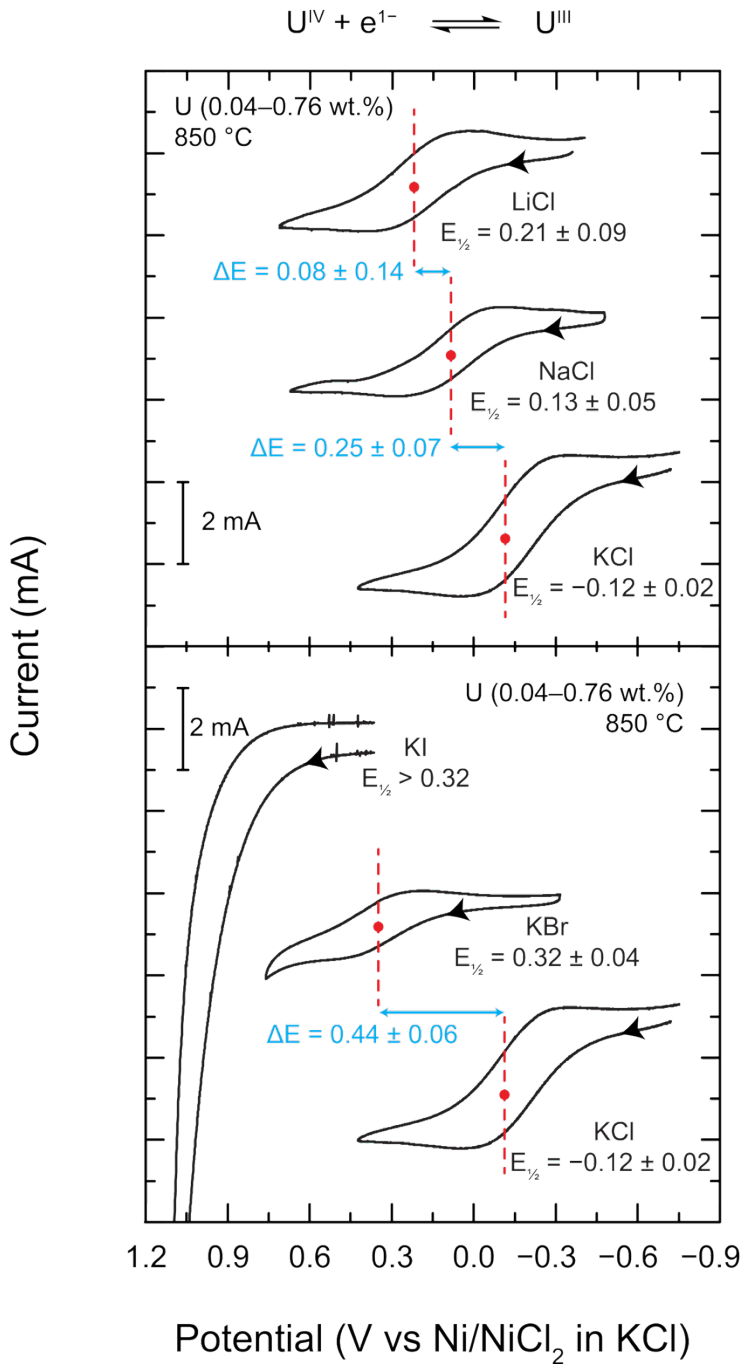

Figure 2. Representative high-temperature cyclic voltammograms (850 °C) of uranium dissolved molten salt solutions. The top pane compares $U^{IV/III}$ data obtained in alkali chloride salts and the bottom pane compares $U^{IV/III}$ data obtained in potassium halide salts (0.04–0.76 wt.% U). The red dots

and dashed lines indicate the average $E_{½}$ value in each salt from three independent measurements with potential differences between pairs of $U^{IV/III}$ redox waves indicated in blue. Data were recorded at a scan rate of 100 mV s^{-1} and references to the $Ni^{II/0}$ redox process as described in the text.

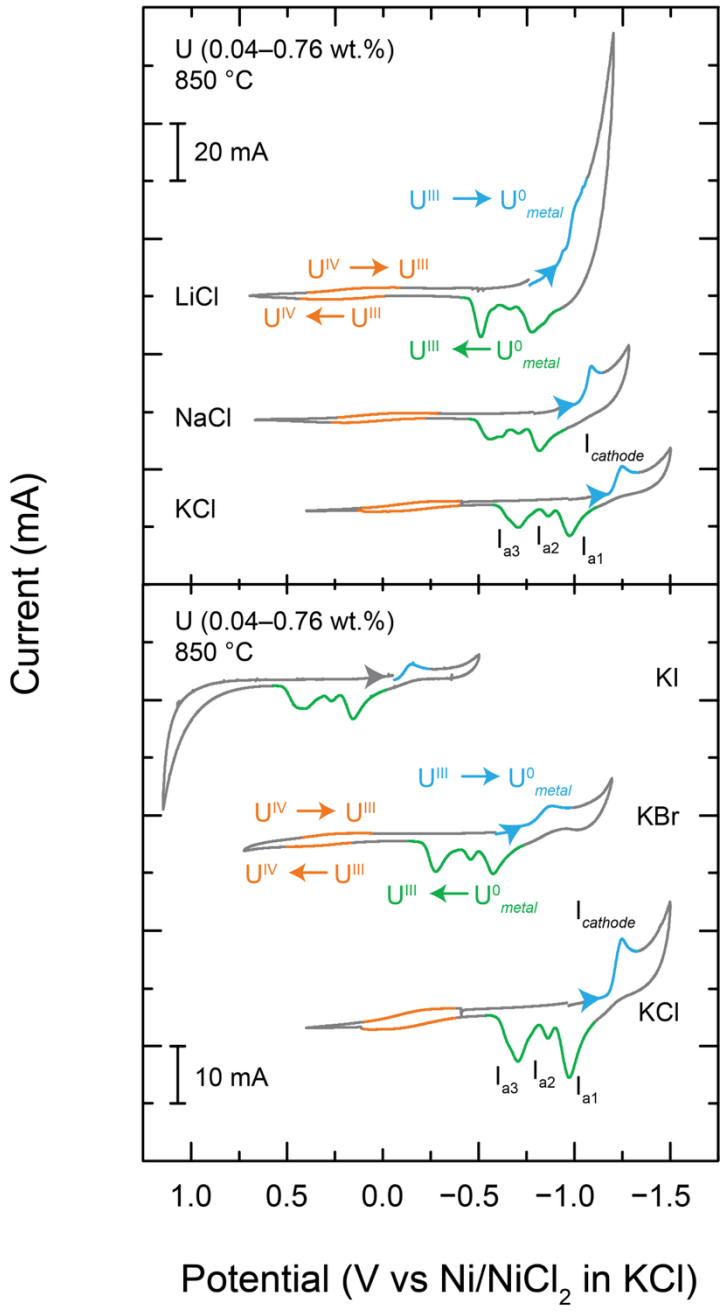

Figure 3. Representative high-temperature cyclic voltammograms (850 °C) from uranium dissolved molten salt solutions. The top pane compares data obtained in alkali chloride salts and the bottom pane compares data obtained in potassium halide salts (0.04–0.76 wt.% U). Features attributed to $U^{IV/III}$ (orange), U^{0}_{metal} deposition (blue; $I_{cathode}$), and stripping (green; I_{a1},

I_{a2}, and I_{a3}) redox processes were labeled accordingly. Data were recorded at a scan rate of 100 mV s^{-1} and referenced to $Ni^{II/0}$ as described in the text.

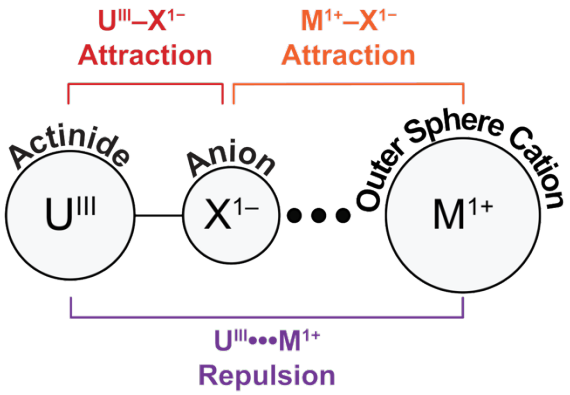

Coulomb's Law

$$F = k\frac{(q_{U^{III}})(q_{X^{1-}})}{r^2}$$

$$F/k = \frac{(q_{U^{III}})(q_{X^{1-}})}{r^2}$$

F=Attractive or repulsive force
K=Constant
q=Charge on atom
r =Distance

$$\Sigma F/k = U^{III}\text{–MX Interaction Parameter}$$

$$U^{III}\text{–MX Interaction Parameter} = \underset{\text{Attraction}}{U^{III}\text{–}X^{1-}} - \underset{\text{Attraction}}{M^{1+}\text{–}X^{1-}} + \underset{\text{Repulsion}}{U^{III}\text{•••}M^{1+}}$$

$$U^{III}\text{–MX Interaction Parameter} = \frac{(q_{U^{III}})(q_{X^{1-}})}{(r_{U^{III}} + r_{X^{1-}})^2} - \frac{(q_{M^{1+}})(q_{X^{1-}})}{(r_{M^{1+}} + r_{X^{1-}})^2} + \frac{(q_{U^{III}} - q_{X^{1-}})(q_{M^{1+}})}{(r_{U^{III}} + 2r_{X^{1-}} + r_{M^{1+}})^2}$$

Scheme 3. Example solvation interaction calculation of U^{III} with a molten salt (MX) in the inner- (left) and outer-coordination spheres (right). U^{III} interacts directly with X^{1-} and the strength of the attractive U^{III}–X^{1-} interaction is reduced by the strength of the interaction between M^{1+} and X^{1-}. The presence of K^{1+} in the outer-coordination sphere creates a repulsive U^{III}–M^{1+} interaction that is reduced by charge screening from X^{1-}. The $U^{IV/III}$ redox process shifts positive in melts containing both large polarizable anions and small polarizing cations, as both help to stabilize the U^{III} oxidation state.

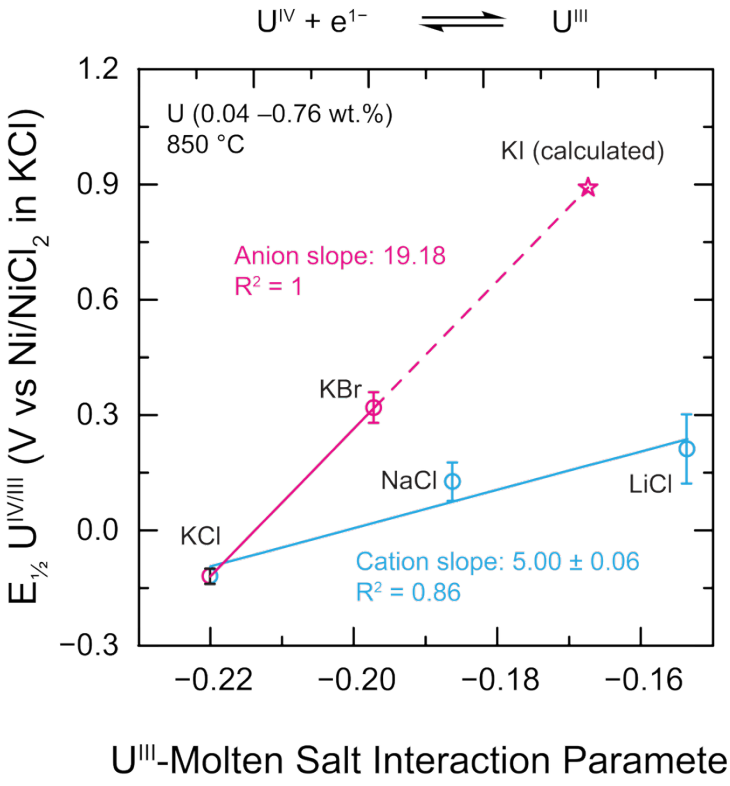

Figure 4. Correlations between $U^{IV/III}$ redox potential and the electrostatic salt interaction parameter at the U^{III} cation in alkali chloride (blue) and potassium halide (magenta) salts. These data were collected in molten salt solutions containing U (0.04–0.76 wt.%) at 850 °C. Linear fits (magenta and blue lines) and slopes for each set of salts are shown. The error bar depicts the standard deviation from the mean (1σ) of the $U^{IV/III}$ $E_{½}$ redox potentials measured in triplicate from three separate molten salt samples. The $E_{½}$ data point in KI was calculated by extrapolating the linear fit of the $U^{IV/III}$ $E_{½}$ redox potentials obtained experimentally in KCl and KBr solutions.

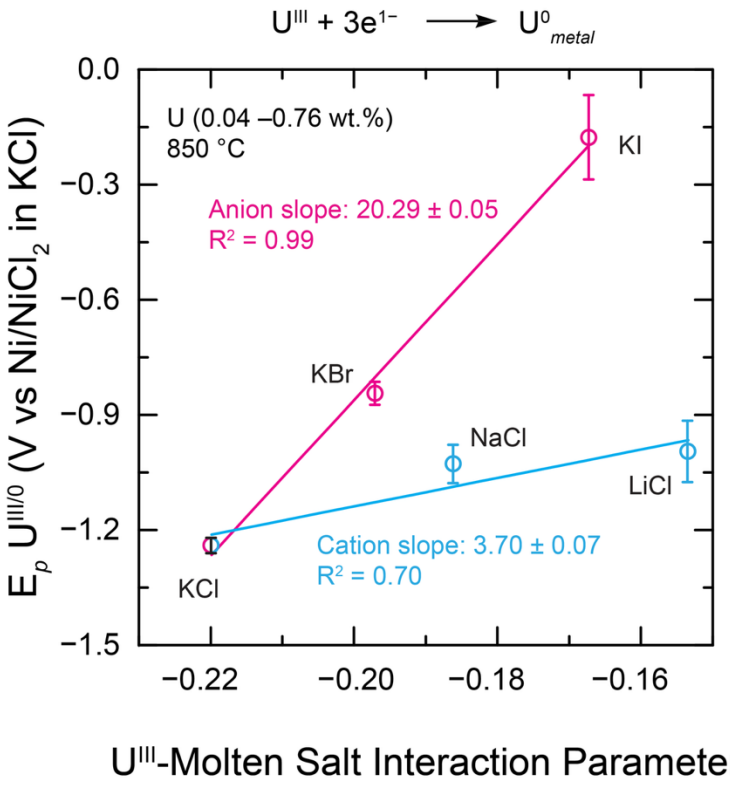

Figure 5. Correlations between U^0_{metal} peak potential (E_p) and the electrostatic salt interaction parameter at the U^{III} cation in alkali chloride (blue) and potassium halide (magenta) salts. These data were collected in molten salt solutions containing U (0.04–0.76 wt.%) at 850 °C. Linear fits (magenta and blue lines) and slopes for each set of salts are shown. The error bars depict the standard deviation from the mean (1σ) of the U^0_{metal} deposition potentials measured in triplicate from three separate molten salt samples.

Table 1. Molten Salts U^{III} Concentrations from Oxidative Stripping of Uranium.

Salt	Observed/Theoretical U^{III} Ratio[a]	Stripping FE%[b]	U^{III} Wt%
LiCl	0.220	22.0	0.220
NaCl	0.041	4.1	0.041
KCl	0.362	36.2	0.362
KBr	0.764	76.4	0.764
KI	0.216	21.6	0.216

[a]Theoretical yield calculated by assuming 100% faradaic efficiency for uranium metal stripping to produce U^{III}. Observed values measured by ICP-AES [b]FE = faradaic efficiency.